Session 2 – EM Design and Measurements

Monday, 11 October 2010

10:00 – 11:30 AM

Session Chair – Dr. Michael J. Havrilla

Air Force Institute of Technology

Dr. Michael J. Havrilla received B.S. degrees in Physics and Mathematics in 1987, the M.S.E.E degree in 1989 and the Ph.D. degree in electrical engineering in 2001 from Michigan State University, East Lansing, MI. From 1990-1995, he was with General Electric Aircraft Engines, Evendale, OH and Lockheed Skunk Works, Palmdale, CA, where he worked as an electrical engineer. He is currently an Associate Professor in the Department of Electrical and Computer Engineering at the Air Force Institute of Technology, Wright-Patterson AFB, OH. He is a member of URSI Commission B, a senior member of the IEEE, and a member of the Eta Kappa Nu and Sigma Xi honor societies. He has approximately 100 journal and conference publications in the field of electromagnetics. His current research interests include electromagnetic and guided-wave theory, electromagnetic propagation and radiation in complex media and structures and electromagnetic materials characterization.

Monday, October 11, 2010
10:00 — 11:30 AM
Session 2: EM Design and Measurements
Chair: Dr. Michael J. Havrilla, Air Force Institute of Technology

10:00	A10-0037: **Side Wall Diffraction & Optimal Back Wall Design in Far-Field Antenna Measurement Chambers at VHF/UHF Frequencies**, John Aubin, Mark Winebrand (ORBIT/FR)
10:15	A10-0040: **Optimization Criterion and Optimal Loading of High Performance Absorbing Materials at VHF/UHF Frequencies**, Mark Winebrand, John Aubin, Per Iverson (ORBIT/FR), Scott Martin (Advanced Electromagnetics, Inc.)
10:30	A10-0049: **Wireless Measurement of UHF RFID Tag Chip Impedance**, Toni Björninen, Mikko Lauri, Risto Ritala (Tampere University of Technology), Atef Elsherbeni, Lauri Sydänheimo, Leena Ukkonen (Univ of Mississippi)
10:45	A10-0074: **Assessment of EMI and EMC Measurement and Calibration Procedures at the National Institute of Standards and Technology**, Lorant Muth, Dennis Camell (NIST)
11:00	A10-0084: **Effectiveness of Loading a Reverberation Chamber - How to Consistently Load Your Chamber**, Jason Coder (Univ of Colorado), John Ladbury, Christopher Holloway, Kate Remley (NIST)
11:15	A10-0117: **Improvement in Low Frequency Test Zone Performance in the Benefield Anechoic Facility**, Lt Christina Jones, James Bartley, Ronnie Fernandez, Michael Shaw (Air Force Flight Test Center)

SIDE WALL DIFFRACTION & OPTIMUM BACK WALL DESIGN IN FAR-FIELD ANTENNA MEASUREMENT CHAMBERS AT VHF/UHF FREQUENCIES

John Aubin & Mark Winebrand
ORBIT/FR Inc., Horsham, PA, 19044
www.orbitfr.com

ABSTRACT

Anechoic chambers utilized for far-field antenna measurements at VHF/UHF frequencies typically comprise rectangular and tapered designs. The primary purpose of conventional far-field chambers is to illuminate a test zone surrounding the Antenna Under Test (AUT) with an electric field that is as uniform as possible, while multiple reflections from the side wall absorber assemblies are kept to a minimum. The cross section dimensions of far field chambers at VHF/UHF frequencies can be electrically small, often as little as 3λ. In this paper the side wall reflections at VHF/UHF bands are studied in more details for elongated rectangular and tapered chambers.

In particular, the reflectivity is evaluated in rectangular chambers as a function of electrical dimensions of the chamber cross – section and of the ratio W (width of the chamber) or H (height of the chamber) to L (length – separation between antennas) for values ranging from 0.5 to 2. The methods of reflectivity improvement are presented and compared. In particular, the conventional chamber design is compared with a "Two Level GTD" approach [4,5,7] and the latter one shows significant reflectivity improvement in the test zone, even at longer source antenna AUT separations.

The side wall reflections are examined in tapered chambers as well. The back wall reflection mechanism, which assumes multiple incident waves – direct from the source antenna and reflected from the side walls, floor and ceiling, is offered and confirmed by the simulation, which, in turn, yields an optimized back wall chamber design (see also [6]).

Keywords: Rectangular Anechoic Chamber, Tapered Anechoic Chamber, VHF/UHF, Side Wall Reflections, "Two Level GTD" method , Optimized Back Wall Design.

1.0 Introduction

Anechoic chambers utilized for far-field antenna measurements at VHF/UHF frequencies comprise primarily rectangular and tapered designs. They typically consist of a shielded enclosure of significant dimensions treated by efficient absorbing materials, and consequently are very costly, with the cost increasing as the lowest operating frequency is reduced. Errors introduced during the construction of such chambers are difficult, expensive or sometimes impossible to correct. As a result, rigorous and accurate 3D electromagnetic (EM) analysis is an important procedure that may be utilized to increase confidence, reduce the risk associated with achieving the desired test zone performance, and to enhance the overall chamber efficiency.

Typically, for a larger test zone, a longer source antenna/AUT separation (L) is required. At VHF/UHF frequencies L must exceed the maximum of $2*D^2/\lambda$, 3D, or 3λ [1], where D is the maximum AUT aperture dimension, and λ is the wavelength at the lowest operating frequency. Accordingly, required chamber dimensions (H/W/L), and in particular the length L, must be increased in order to meet this criterion. This in turn may increase the level of reflections from the side walls, floor, and ceiling, which negatively contribute to the desired uniform test zone illumination.

Note that the cross section dimensions of the elongated chambers at VHF frequencies can be electrically small, often as little as 3λ. This increases the reflections even more, as the side wall absorber performance at oblique, low angles of incidence deteriorates more rapidly at lower frequencies [2,3]. In addition, the attenuation of the reflections due to free space propagation in the chamber is a negligible contributing factor at VHF/UHF frequencies, which is not the case in chambers operating at frequencies significantly above 1GHz. As a result, the test zone performance may be unacceptable, although it is not always readily detectable.

2.0 Reflections in Elongated Rectangular Anechoic Chambers

The most critical manifestation of unsatisfactory test zone performance can be observed in rectangular chambers designed for operation at the VHF/UHF bands using a classic 60 degree side wall specular incidence angle ($W/L \approx H/L \leq 0.5$). Figure 1(reproduced from [3]) illustrates the difference between the measured received direct signal from the source antenna (**BLUE** and **ROSE**) and the reflected signal (**YELLOW** and **dark BLUE**) from the walls of the chamber in the center of the test zone for two orthogonal polarizations. As is evident, the level of reflections at low frequencies exceeds the direct signal, thus demonstrating that there is very limited absorption on the side walls at VHF. The chamber in effect behaves

like a "tube" at low frequencies, with the reflectivity monotonically decreasing with frequency.

The reflectivity in this chamber at the lowest operating frequency, where W,H ≈ 4λ, is ~+12dB. In addition, Figure 1demonstates less than desirable chamber performance in the range W,H ≈ 8-10λ, where the direct and reflected signal are essentially equal. The reflectivity becomes more acceptable for conventional antenna measurements, e.g. <-15dB, at higher frequencies, where W, H exceed 14λ. The reason the Free Space VSWR test results performed in the chamber appeared acceptable at VHF/UNF frequencies is that the VSWR processing inevitably interpreted the dominant reflected signals as the direct one, leading to incorrect conclusions regarding chamber performance.

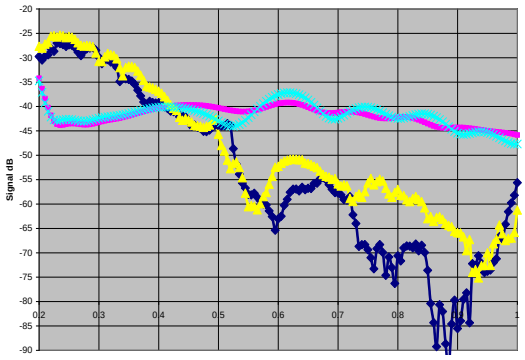

Figure 1. Direct and Reflected Signals for the Chamber with W/L≈H/L≤0.5 for two Orthogonal Polarizations.

The table below summarizes findings on test zone reflectivity at VHF/UHF frequencies (measurements and simulations) for different chamber geometries and electrical dimensions.

W = H ≈ Xλ **W/L = H/L≈ Y**	**X=3**	**X=4**	**X=7**	**X=17**
Y=0.5		**+12dB**		**-15dB**
Y=1.0	**+3dB**		**-20dB**	
Y=2.0	**-20dB**			

From the above table the conclusion is drawn that the reflectivity in an elongated rectangular chamber can be improved using one or a combination of the following approaches:

a) Increasing the grade and size of the absorbing materials applied to the side walls (a very expensive approach at VHF/UHF frequencies – implementation is described in [2,3])
b) Increasing W and H (a very expensive approach – implementation is described in [2,3])
c) Reducing the length L (this may reduce test zone dimensions, and additional attention must be paid to mutual and reactive coupling between the AUT and source antennas – implementation is described in [2,3])
d) Reducing the beamwidth of the source antenna – implementation is described in [2,3]
e) Implementing the "Two–Level GTD" method [4,5,7] in the design of side walls to minimize the effect of reflections on the test zone (described in more details in the section 3 below)
f) Implementing the back wall design in accordance with [6,7] (see also section 4.0 of this paper. This would reduce the effect of back wall reflections on the test zone)

3.0 "Two – Level GTD" Method of Reflection Reduction in the Test Zone of Elongated Rectangular Chambers

The "Two–Level GTD" method has been introduced in [4,5,7] and is shown to improve significantly the test zone performance /reflectivity as compared to a conventional chamber layout. In particular, performance improvement has been demonstrated in an example of a chamber operating at 2 GHz and above. The longitudinal probe cuts of the field in a conventional chamber layout, in a chamber with inverted "open book" metallic side walls, floor and ceiling treated with conventional pyramidal absorbing materials, and in a chamber with inverted "open book" metallic side walls, floor and ceiling treated with a "fishbone" wedge absorber layout are shown on Figure 2.

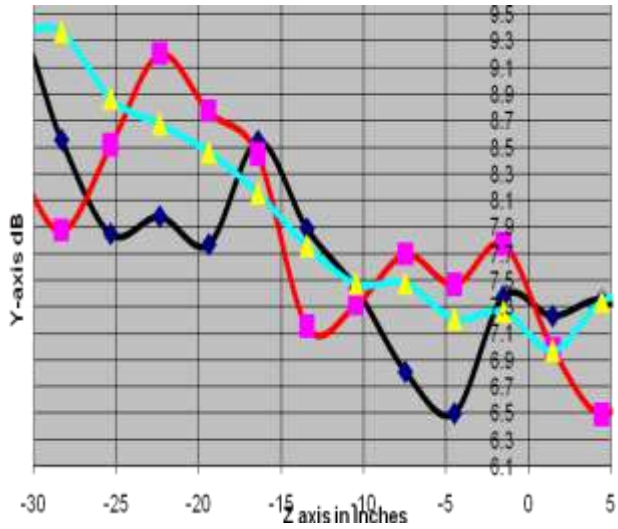

Figure 2. Longitudinal cuts @ 2.0 GHz. Black –Flat Side Walls Lined with 24" Pyramid Absorber; Red – Inverted "Open Book" Side Walls Lined with 24" Pyramid Absorber; Blue – Inverted "Open Book" Side Walls Lined with a "Fishbone" 24" Wedge Absorber

The improvement in the reflectivity of a chamber with a "fishbone "absorber layout is clearly observed in Figure 2. One should note, however, that the example chamber geometry was comprised of side walls, floor and ceiling with characteristic electrical dimensions of about 35λ – an aperture large enough to assume with a high probability that GO and GTD postulates are satisfied and , therefore, the " Two Level GTD" method is valid. The question, which remains unanswered is - Could the method be applicable at low frequency chambers with the side wall dimensions as electrically small as 3λ? In order to answer this question the following example is considered in a 3D EM simulation below: the chamber external dimensions are 33' (L) x 20' (W) x 20' (H).

In one model a flat chamber side wall is treated by conventional 48" diamond patch pyramidal absorber - see Figure 3a), and in the other model the side wall backing plate is arranged as an inverted "open book" and the side wall is treated by a "fishbone" absorbing layout made of 48" wedge absorber – see Figure 3b). The back wall in both models was replaced by perfect absorptive boundary conditions. This is done to evaluate the difference due to the side wall chamber arrangement only. The simulation frequency is 150MHz. The comparative simulation was done using a 15' source antenna/AUT separation, and with a relatively high gain source antenna (8-9dBil). In addition a low gain source antenna was considered in the "fishbone" model. The simulation results are presented in Figures 4 and 5.

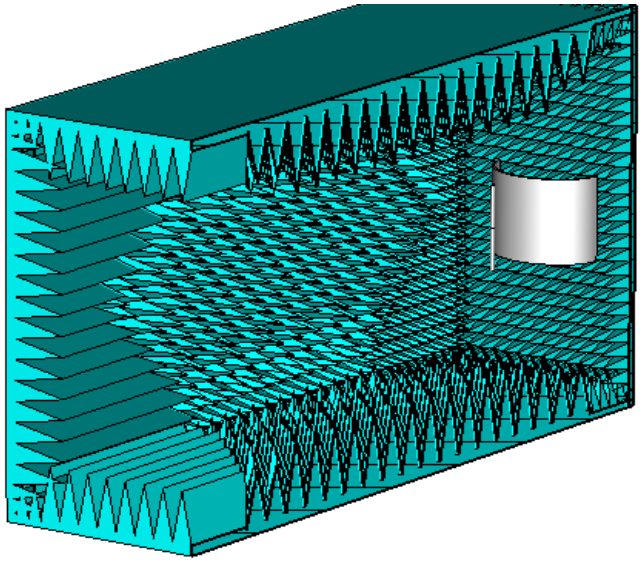

a)

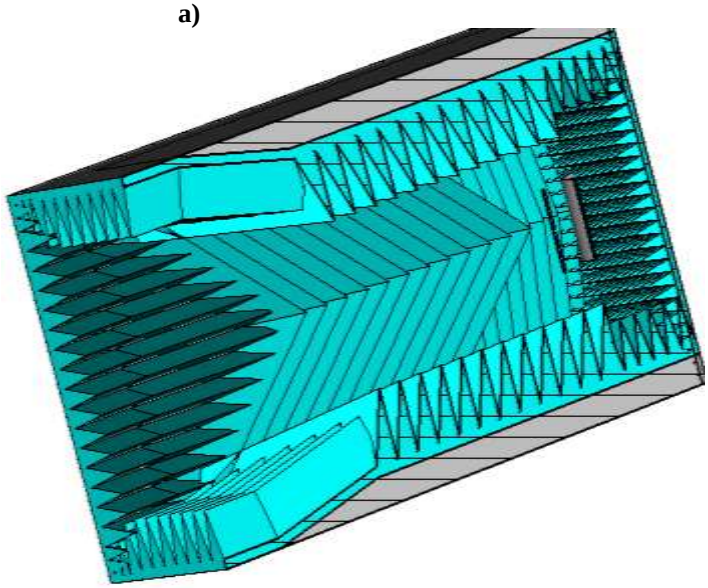

b)

Figure 3. a) Conventional Chamber Layout
b) "Fishbone" Chamber Layout

Contour plots of the electromagnetic field in a transversal plane passing thru the center of the test zone are shown on Figure 4a) and 4b), respectively. It is evident that the uniformity of the field in the test zone is much better for case b). The longitudinal cuts for both chambers are shown in Figure 5. It is shown that the reflectivity is improved from less than 20 dB to 23dB in the conventional chamber (**Blue** curve) to better than 30dB in case b) (**Green** curve). In addition, it is evident from Figure 5 that side walls control reflections in the chamber with a "fishbone" layout so effectively, that even a low gain source antenna does not degrade the reflectivity (**RED** curve) as compared to use of a "high" gain source

antenna (**GREEN** curve), as the curves (**GREEN** and **RED**) are very similar.

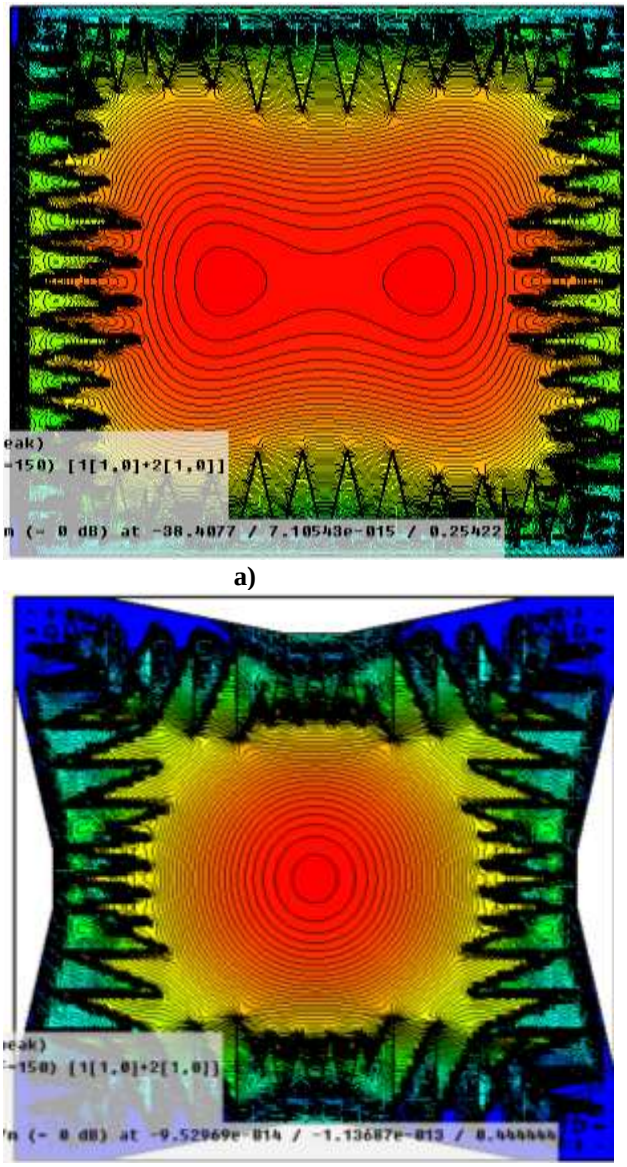

a)

b)

Figure 4. Contour Plots of the Magnitude of the Electric Field in the Test Zone @ 150 MHz
a) Conventional Chamber Layout
b) "Fishbone" Chamber Layout.

4.0 Reflections in Elongated Tapered Anechoic Chambers

Though tapered anechoic chambers are generally considered to be better candidates for VHF/UHF antenna measurements, the reflectivity in the chamber is still considered to exhi9bit a serious influence on test zone performance. In the simulations below a generic tapered chamber, treated with flat absorbing material, is studied.

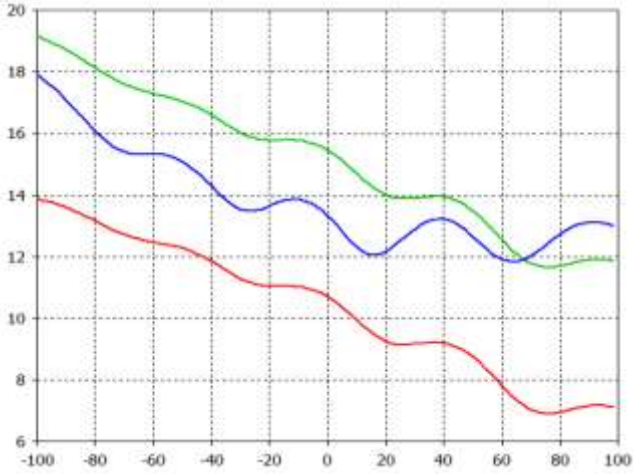

Figure 5. Longitudinal cuts @150 MHz
BLUE – Cut in the chamber with conventional layout
GREEN – Cut in the chamber with a "fishbone" layout & "high" gain source antenna
RED- Cut in the chamber with a "fishbone" layout & low gain source antenna

In order to separate the reflections from the side and back walls, the simulation, with results presented in Figure 6, was intentionally performed with an "open" back wall. The longitudinal cuts along the chamber axis are shown for cross section dimensions W, H ≈ 4λ, 5λ, and 6λ. It is clearly seen that the field unexpectedly rises by ~2dB at the back opening of the chamber for W, H ≈ 4λ , then is reduced to <1dB for W, H ≈ 5λ, and the rise is eliminated totally for W, H ≈ 6λ. Although the field growth region is located behind the region of interest (i.e., the test zone), and therefore does not directly affect the test zone, it increases and complicates the incident field on the back wall.

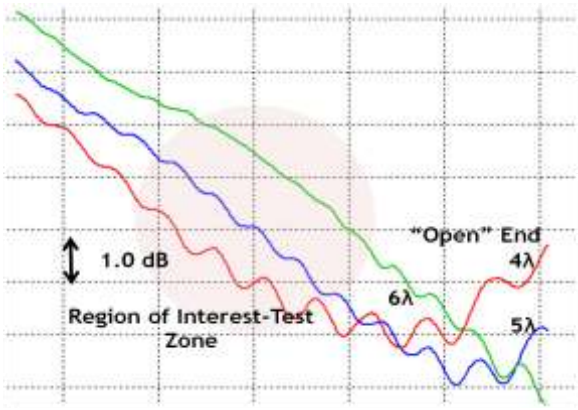

Figure 6. Longitudinal Cuts in a Tapered Anechoic Chambers with "Open" Back Wall

In Figure 7 longitudinal cuts are shown in a tapered anechoic chamber for an "open" back wall (**GREEN** curve), which is considered to be a reference, for a flat metallic back wall with no absorbing material (RED curve), and for a pyramidal metallic shaped back wall with no absorbing material (**BLUE** curve). If we assume that only a spherical wave is generated in the tapered chamber and is incident on the back wall, then the standing wave created by the incident and reflected signals would not exceed the incident signal by more than 4.5dB in the region of interest (test zone), vs. 6 dB in the simulation (the distance from the test zone to the back wall is typically ~L/3).

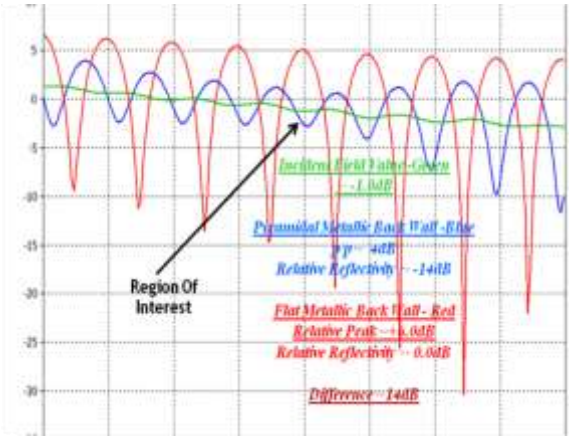

Figure 7. Longitudinal Cuts in the Tapered Anechoic Chambers with "Open" (green), Flat Metallic (red), & Pyramidal Metallic (blue) Back Walls

This would imply that there are more than one incident/ reflected waves, and that the contributing incident waves may include the diffracted waves from the side walls as shown in Figure 8(a).

5.0 Optimum Back Wall Design in Elongated Chambers

The diffraction mechanism suggested in section 4 naturally leads to an optimized shaped back wall design, discussed in more detail in [6,7] and shown in Figure 8(b). The **BLUE** curve in Figure 7 shows the longitudinal cut in a tapered chamber with a pyramidal metallic back wall. It provides ~4dB peak/peak level of oscillation around the reference incident field (**GREEN** curve), which translates into ~14dB of reflectivity improvement versus a flat metallic wall. Assuming that the absorber applied to the back wall improves nearly identically the reflectivity of the flat and pyramidal walls, the optimized back wall design is at least comparable with the approach suggested in [8], and presents a significantly less costly approach.

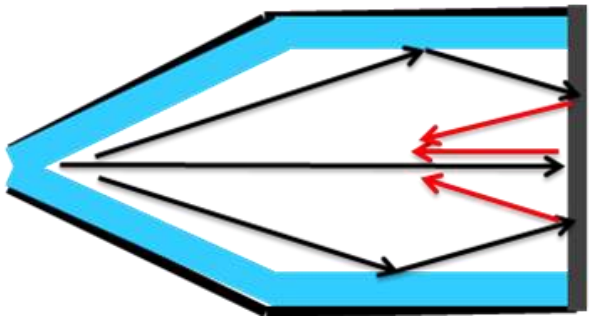

a)

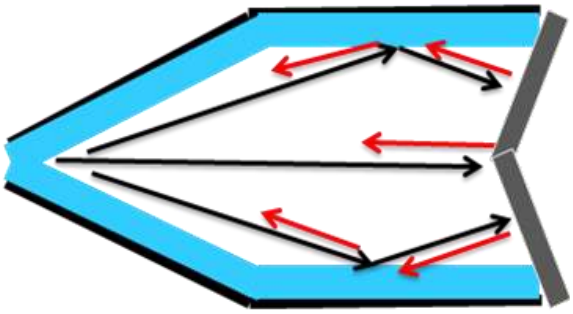

b)

Figure 8. Diffraction Mechanism in a) Elongated Anechoic Chamber and b) Optimum Back Wall Design

6.0 Conclusions

Side wall diffraction has been studied in elongated rectangular and tapered anechoic chambers at VHF/UHF bands. Methods for diffraction reduction in rectangular chambers were suggested.

It is shown that a "Two- Level GTD" method supersedes other methods in that it:

- Reduces more effectively the reflectivity in the test zone at VHF/UHF frequency bands

- Allows a longer source antenna/AUT separation with better reflectivity in the test zone at VHF/UHF frequencies

- May not require a higher gain source antenna (conventional low gain antennas can be used as a source antenna) to better control the reflectivity in the test zone at VHF/UHF frequencies

- Though the method is based on GTD postulates, it is shown that the method can be effectively implemented down to low frequencies, where the side wall characteristic dimensions can be electrically small as 3λ

The incident wave structure on the back wall has been studied at the lowest operating frequencies in tapered chambers. It has been shown that:

- Multiple incident waves, rather than a single spherical wave, are incident on the back wall of the chamber at the lowest operating frequencies, where the side wall characteristic dimensions are typically between 3λ to 4λ.

– A pyramidal shaped metallic back wall treated with conventional absorbing materials represents the optimum and most cost effective solution

- Expected back wall reflectivity improvement of at least 10 dB can be achieved in chambers with a pyramidal metallic back wall

7.0 REFERENCES

[1] CTIA Certification. Test Plan for Mobile Station Over the Air Performance Test, December 2008.

[2] M. Winebrand, J. Aubin. Test Zone Performance in Low Frequency Anechoic Chambers. Microwave Journal, October 2008, pp.140-148

[3] M. Winebrand, J. Aubin. Test Zone Performance in Low Frequency Anechoic Chambers, Proceedings of the AMTA 2008, pp. 482-488.

[4] M. Winebrand, J. Aubin and M. Boumans. A Two-Level GTD Utilization in Designing Anechoic Chambers For Antenna Measurements, IEEE APS Proceedings 2009.

[5] M. Winebrand, J. Aubin and M. Boumans. Test Zone Performance Enhancement In Anechoic Chambers Using Two – Level GTD Principles, Proceedings of the AMTA 2009, pp. 92-97.

[6] J. Aubin, M. Winebrand. Back Wall Design Trade-Offs In High Performance VHF/UHF Chambers, Proceedings of the AMTA 2009

[7] M. Winebrand & J. Aubin. Absorber Assembly for an Anechoic Chamber. US Patent Pending PCT/US2009/062473.

[8] W.D. Burnside, et al. Tapered Anechoic Chamber. US Patent 6,437,748.August 20, 2002.

OPTIMIZATION CRITERION AND OPTIMUM LOADING OF HIGH PERFORMANCE ABSORBING MATERIALS AT VHF/UHF FREQUENCIES

Mark M. Winebrand, Ph.D.[(1)] , John Aubin [(1)] , Scott Martin[(2)] and Per Iversen[(1)]
(1) ORBIT/FR Inc., Horsham, PA, 19044
(2) Advanced Electromagnetics, Inc. , Santee, CA 92071

ABSTRACT

This paper describes the principles of operation of high performance absorbing materials and the criterion for its performance optimization at UHF/VHF frequency bands. The optimization criterion is intended to determine the optimum carbon loading of the foam based absorber components, thus delivering optimal reflectivity of the full absorbing assembly (foam based absorber components on a metallic backing plate) at the lowest possible operating frequency. The optimization is based on equalization of reflections in the time-domain from the front face surface of the absorbing component and from the backing metallic plate. Validity is confirmed by measurements of the reflectivity of pyramidal absorbing components of varying heights, (3', 5', 6' and 8') in a 40' long coaxial line terminated in a metallic back wall.

In addition, it is shown that the "aging" process of the absorbing components can be characterized by the change of the effective reflectivity in the time-domain of the components as a function of aging time. It is possible to determine whether the absorber performance is stabilized and the "aging" process is complete, and whether the loading of the absorber carbon mix is optimum, or is otherwise under-loaded or over-loaded. In particular, it is possible to determine prior to the time when the "aging" process is stabilized whether the loading is excessive.

Keywords: Absorbing Materials, Absorbing Assembly, Reflectivity, Time – Domain, Aging.

1.0 Introduction

Typical anechoic chambers for EMC, Far–Field, Near-Field antenna or RCS measurements comprise a metallic enclosure with internal surfaces covered by absorbing foam based material, conventionally composed of pyramidal, wedge or similar shapes. It is common for antenna engineers to make the following assumptions regarding the performance of microwave anechoic absorber materials:

- Absorbing material reflectivity is monotonically improving if larger absorbers (e.g., larger pyramid heights) are used
- Reflectivity of larger absorbing materials is better at lower frequencies, allowing the extension of the operating frequency band of the absorber and chamber to a lower frequency.
- Absorbing material reflectivity is improved if a higher carbon loading is impregnated into the materials

In this paper it is demonstrated that these assumptions may not be applicable to the absorbing materials commonly used at VHF/UHF frequency bands. If the chamber operates down to VHF/UHF frequencies, then the height of foam impregnated absorber components may vary from 0.9m up to 2.4m or more. The reflectivity of these absorbing materials is critical at VHF/UHF, as the chamber cross-section may span only a few wavelengths at these frequencies, and the free space propagation loss of the waves reflected off the absorber is no longer a significantly enhancing factor to aid in the overall chamber reflectivity. Moreover, manufacturing of such absorbers is expensive and challenging for VHF/UHF frequencies.

A variable carbon based loading as a function of absorber height may be implemented in the design to achieve superior performance at lower frequencies, and a simple criterion that can be readily implemented in the manufacturing process, and which delivers optimum loading/reflectivity, is important in the practical implementation of VHF/UHF chambers. Such a criterion is formulated in the paper. The criterion is based on equalization of the level of reflections in the time domain from the face surface of the absorbing component and from the backing metallic plate, and its validity is confirmed by a series of absorber reflectivity measurements and optimization in a coaxial line [1], [2].

Another issue associated with high performance absorbers is the "aging" process – the time period necessary after absorber manufacturing to achieve its stable and final performance. Taller absorber in general requires a longer "aging" period. It can last several months for absorber components of a height of 8' or taller. It is shown in the paper that the reflectivity of the absorbers is changing with "age" from an "under-loaded" towards an "over-

loaded" condition in time-domain reflectivity plots. Thus, it is always possible to determine by measurements if the "aging" process is stabilized or not, unlike in the frequency domain, where the measured reflectivity does not necessarily indicate the stage of the "aging" process. In particular, it is possible to identify if the absorber is overloaded prior to completion of the "aging" stabilization time, thus saving time on absorber optimization and manufacturing.

2.0 Dielectric Properties of Foam Based Absorbing Materials

Dielectric properties of foam based absorbing materials are determined by the carbon mix impregnated into the foam, and can be modified depending on the carbon percentage in the mix - c_p. The dielectric properties versus frequency are well described by the formulas:

$$\varepsilon'(f) = a'(c_p)/f + b'(c_p) \qquad (1')$$

$$\varepsilon''(f) = a''(c_p)/f + b''(c_p) \qquad (1'')$$

where: f is the operating frequency, $1.5 \le b' \le 2.5$, $b'/2 \le b'' \le b'$ and a', a'' & b', b'' are monotonically increasing functions of the carbon mix percentage c_p. The parameters $\varepsilon'(f)$ & $\varepsilon''(f)$ can reach values > 20 at VHF frequencies.

From formula (1) it is easy to conclude that the impregnation carbon mix value c_p and its accuracy are not critical at higher frequencies, as the dielectric constants are independent of frequency and converge at $f \Rightarrow \infty$ to very stable values. Therefore, the reflectivity of absorbing materials is independent of the loading and is essentially determined by the absorber shape. However, the impregnation value and accuracy are very important at VHF / UHF frequency bands, where the reflectivity depends strongly on the dielectric properties of the absorbers and, unlike at higher frequencies, is less dependent on the absorber shape.

It is the target of this paper to optimize the absorber reflectivity at VHF/UHF frequency bands. As this does not lead to ambiguities, and since the parameters a', a'' & b', b'' are monotonic functions of c_p, it is convenient, instead of using formula (1), to characterize the dielectric properties of the absorber by the percentage of the carbon mix c_p. It is also more convenient in determination of the optimization criterion for the absorber performance, and of the parameters to be optimized.

3.0 Absorption vs. Reflection in Absorbing Materials

Reflections occur at the border between air and dielectric absorptive media as shown in Figure 1a), where a normal incidence angle of the incident wave is assumed. Based on the values of b', b'' in (1), it is easy to conclude for practical values that the reflection coefficient cannot be better than approximately -15 dB.

Note that in practical chambers such reflection levels may negatively contribute to the overall chamber reflectivity, regardless of the rate of absorption of the penetrated wave inside of the dielectric media, and is much worse than typically stated performance values of various commercial absorbing materials, which are often specified down to -55dB (see for example [2]). The reflection can be further reduced if a metallic plate (e.g., a shielded chamber wall) is added at a distance - d from the dielectric–air border as shown in Figure 1b). The addition of the metallic plate provides with a new performance contributor, as the two reflections from the border and from the metallic plate can be configured such that they cancel out each other, if a proper distance $-d$ and the carbon mix loading c_p are chosen. Unfortunately, this cancellation is narrow band because of the wavelength dependent spacing required to achieve the 180 degree phase difference necessary to cancel these reflections.

In order to increase the bandwidth of the cancellation, a shaped border can be implemented, as is shown in Figure 1c), where the shaping is chosen to be similar to conventional pyramidal absorbing materials. This absorbing assembly conceptual reflection model leads to the conclusions that the performance of the absorber is completely characterized by the following three factors:

- Scattering from the front face of the absorber assembly
- Reflections from the backing metallic plate
- Absorption inside of the loaded foam

In order to optimize the absorber performance at normal incidence, additional conditions must hold. One additional condition (in addition to a 180 degree phase difference) for optimal absorber behavior (i.e., minimum normal incidence reflectivity) is that the magnitudes of the reflections from the shaped border and from the metallic plate are approximately equal at a distance - d_{eff} of the "effective planar" border from the metallic plate. This is a necessary condition for the cancellation of the two reflections.

Unfortunately, it is not obvious, if possible at all, to:

- correctly identify d_{eff}
- validate that the two reflections are equal

Instead, in this paper we offer a different approach in which is:

For a given height and shape of the absorbing material, the optimum carbon loading (percentage) c_p leading to the optimum (lowest) reflectivity of the absorbing

assembly(absorbing components on a metallic backing plate) at normal incidence can be achieved by equalizing the two reflections from the front face and from the metallic backing plate of the absorber assembly in the time domain.

Absorber properties are typically considered over a broad range of frequencies, since in general an anechoic chamber is desired to be utilized as a broad band measurement facility. Therefore, the time domain is a natural technique to analyze absorber performance. In particular this technique (frequency domain transformation to the time domain and back) is an inherent part of signal processing in tapered coaxial lines utilized for broadband absorbing material characterization, as it is used to eliminate unwanted higher order modes with time gating [1,3]. In the following section the criterion will be justified by a number of absorber material measurements performed in a coaxial line [1], and, as will be shown, can be utilized to optimize absorbing material loading and reflectivity performance.

4.0 Reflectivity and Optimal Loading of Various Absorber Sizes

In Figure 2 the reflectivity of absorbing pyramids of 3'and 5' height are presented in the frequency and time domain – Figures 2a) and 2b) respectively. Both absorbers were impregnated using a carbon mix corresponding to c_p= 24%. The measurements were made using a 40' long rectangular coaxial line, in which the reflectivity measurements from the absorbers were compared to the reflections in the coaxial line when terminated in a short [1]. The figure shows that, as expected, the reflectivity of 5' tall pyramids is significantly better over a broad range of frequencies than for the 3' tall pyramids, and that its operation extends to lower frequencies.

Figure 2b) indicates that, according to the criterion formulated in section 3, both absorbers are optimally loaded and, therefore, optimally designed, as the reflection from the metallic backing (whose peak is near **0ns**) is essentially the same as that from the face of the absorber. However, the reflectivity of 6' tall pyramidal absorber with the same loading is noticeably worse than of the 5' tall pyramids, as indicated in Figure 3a) (blue curve), and the absorber is over-loaded as indicated in Figure 3b), as a much higher reflections occur at the front face of the absorber than at the rear metallic plate.

On the other hand, the same absorber loaded using c_p =15% is, as indicated in Figure 3b), is under-loaded, as the majority of the reflections occur from the backing metallic plate. Note that the reflectivity in the frequency domain is nearly identical for both loadings ***c_p= 15% and c_p= 24% ,*** as can be easily seen in Figure 3a), while it can be clearly distinguished and classified in time – domain as under- loaded versus over-loaded, as can be easily seen in Figure 3 b). The latter means that both loadings are not optimal, and that there is an optimal loading in between these values. Indeed, the red reflectivity curve on Figure 3a), which corresponds to **c_p =17 %,** exhibits much better reflectivity than the other two, and as can be seen from Figure 3b), is nearly optimal, as the reflections from the front face of the absorber and from the backing metallic plate are nearly equal in magnitude. Thus, it can be readily concluded that these measurements confirm the validity and usefulness of this criterion for absorber performance optimization.

5.0 Optimization and "Aging" of 8' Pyramidal Foam Absorber

Extrapolation of the measurement results and of the optimum loading values from 3', 5' and 6' tall absorbers to an 8' tall absorber indicate the optimal c_p value to be below 15%. Indeed, the results of the measurements of 8' tall absorber pyramids loaded by c_p =15% show slightly over-loaded reflectivity in the time – domain. Thus, reduced loading is necessary for a better/optimized reflectivity performance. However, in order to approach the optimum performance, and verify the optimum loading, the absorbing material should be manufactured and then "aged" or cured until its performance is stabilized.

The performance of c_p =13.5% loaded 8' pyramids was tested once a week after it was manufactured and results are presented on Figure 4 for the tests performed on 1st , 2nd and 3rd weeks and on Figure 5 for the tests performed on 7th and 8th weeks. As one can observe, the reflectivity varies and changes every week until it is stabilized (see weeks 7 and 8 in Figure 5). During the 1st week the performance/reflectivity indicates an under-loaded condition, and then it changes consistently with time toward an over-loaded condition (see weeks 1,2, and 3 in Figure 4).

If the loading is optimum, the performance is stabilized at a balanced condition, where the optimum criterion is satisfied as shown in Figure 5a), b). Note, that the "optimal" achieved reflectivity is as low as -35dB or even lower everywhere at frequencies higher than 100 MHz, and that the "aging" period is about two months. If, however, the loading would not be the optimum, then the performance could be, for example, an over-loaded condition even before the stabilization time is reached.

This fact can be utilized to reduce the time necessary to find the optimal loading. Another useful property of the measurements in the time – domain is that the stabilization time or "aging" period can be clearly

determined as the trend with time is from an under-loaded to an over-loaded condition, while in the frequency domain ambiguity is possible.

6.0 Summary

An efficient, easy to implement criterion for the optimal design of microwave absorbers at VHF/UHF frequencies is formulated in terms of reflectivity in the time domain, and validated based on the reflectivity measurements of various size absorbing pyramids at VHF/UHF frequencies in a coaxial line [1].

Based on the criterion, the optimum loading of 8' pyramids is found to be 13.5%. Better than -35dB reflectivity was measured at frequencies higher than 100 MHz. In addition the "aging" process of absorbing materials was studied, and it is shown that the "aging" process can be characterized by the change of the effective reflectivity of the components in the time-domain. It is possible to determine whether the absorber performance is stabilized and if the "aging" process is complete, and whether the loading of the absorber is optimum or, otherwise, under-loaded or over-loaded.

In particular, it is possible to observe prior to the time that the "aging" process is stabilized whether or not the loading is excessive. It is shown that the "aging" of 8' absorber pyramids is lasts approximately 2 months.

References

[1] VHF/UHF High Performance Absorbing Material Measurements in a Coaxial Line Using Time-Gating Techniques. Validation & Error Analysis. Gabriel Sanchez, Mark Winebrand, Vadim Vinogradov and Leland Hemming. Proceedings AMTA 2007. St. Louise. 2007

[2] ORBIT/FR Product Catalog. www.orbitfr.com

[3] IEEE Std 1128-1998."IEEE Recommended Practice for Radio-Frequency (RF) Absorber Evaluation in the Range of 30 MHz to 5.0 GHz".

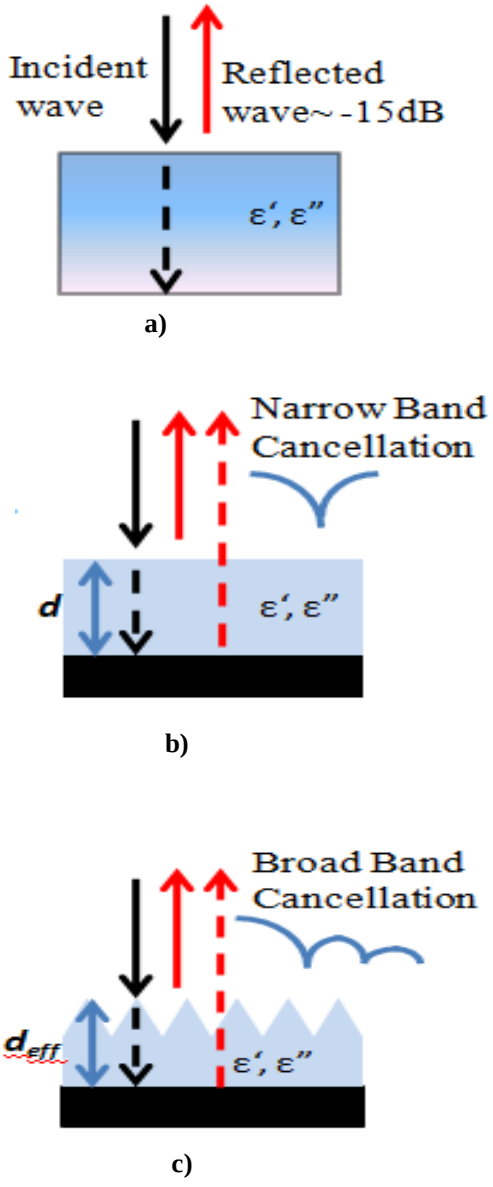

Figure 1. Reflections in an absorbing assembly: a) on the border between two media – air and absorptive dielectric; b) on the border and on a metallic backing plate at a distance – *d*; c) on a shaped border and on a metallic backing plate at the distance – d_{eff}

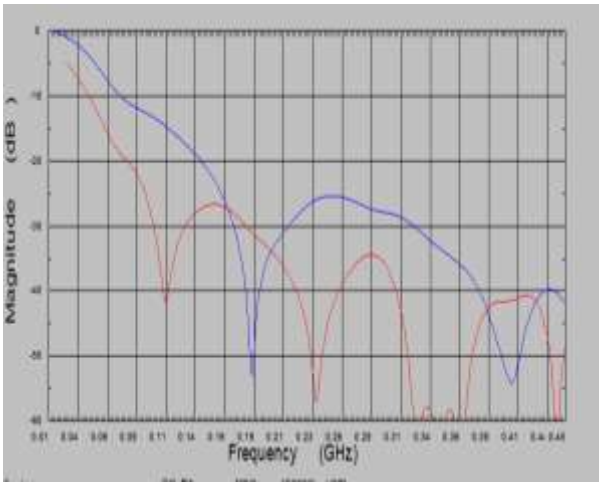

a)

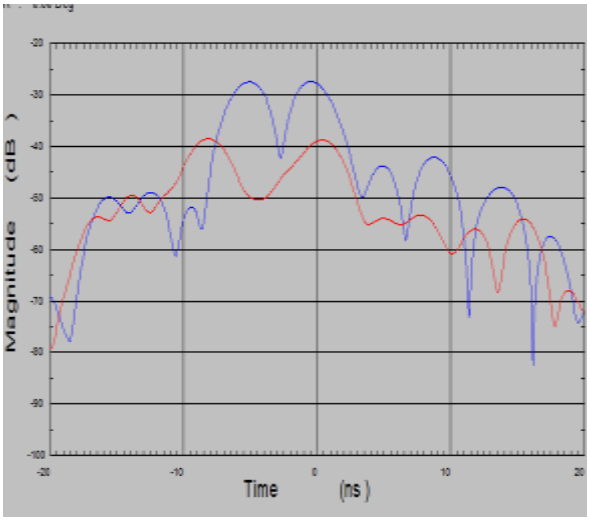

b)

Figure 2. c_p =24%; a) Frequency-Reflectivity of 3'(blue) and 5'(red) absorbers; b) Time-Domain Reflectivity of 3'(blue) and 5'(red) absorbers

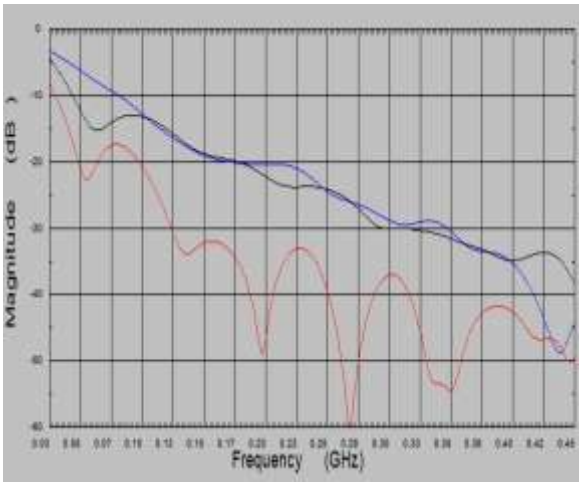

a)

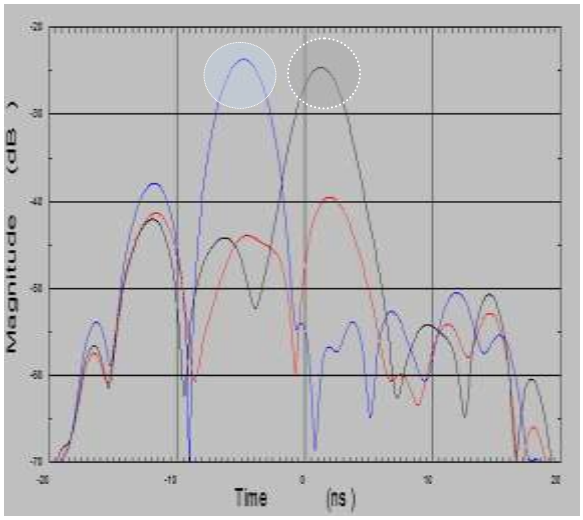

b)

Figure 3. a) Frequency-Domain Reflectivity of 6' tall absorbers with c_p =15% (black), 17% (red) and 24% (blue); b) Time-Domain Reflectivity of 6' tall absorbers with c_p =15% (black), 17% (red) and 24% (blue)

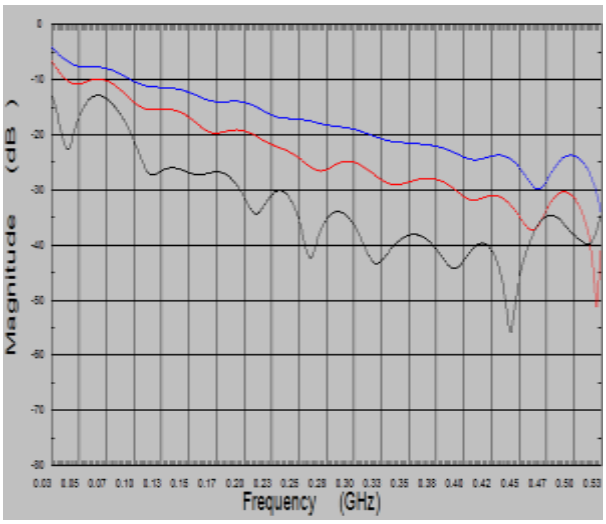

a)

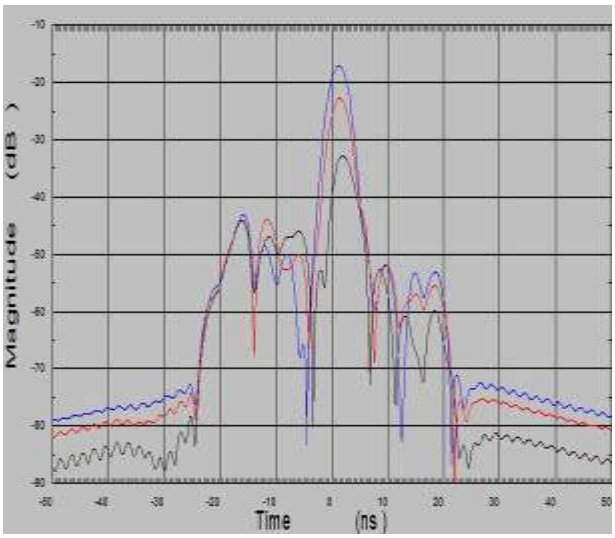

b)

Figure 4. Loading c_p =13.5%; a) Frequency-Domain Reflectivity of 8' tall absorbers measured after 1st, 2nd & 3rd weeks, respectively, after manufacturing; b) Time-Domain Reflectivity of 8' tall absorbers measured after 1st, 2nd & 3rd weeks, respectively, after manufacturing.

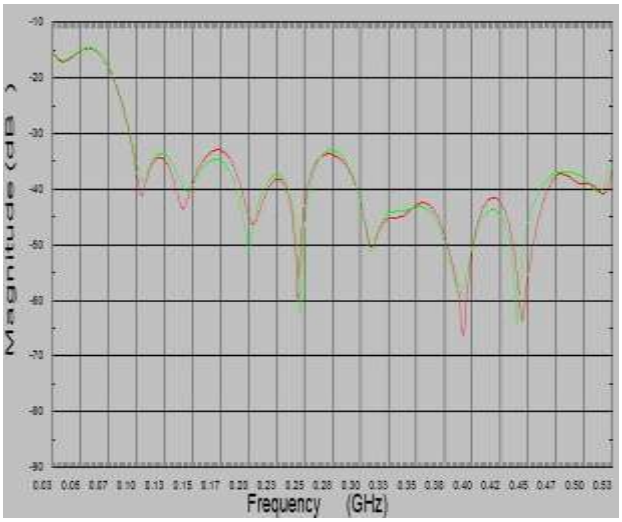

a)

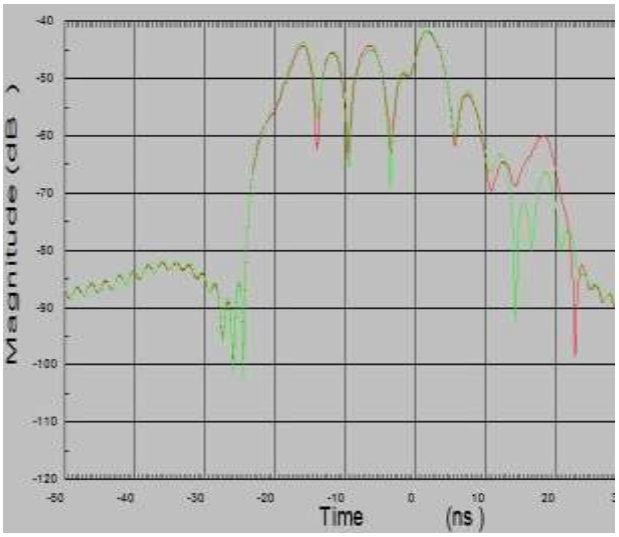

b)

Figure 5. Loading c_p =13.5%; a) Frequency-Domain Reflectivity of 8' tall absorbers measured after 7th and 8th weeks, respectively, after manufacturing; b) Time-Domain Reflectivity of 8' tall absorbers measured after 7th and 8th weeks, respectively, after manufacturing.

WIRELESS MEASUREMENT OF UHF RFID TAG CHIP IMPEDANCE

Toni Björninen, Leena Ukkonen, Lauri Sydänheimo
Department of Electronics
Tampere University of Technology
Kalliokatu 2, FI-26100 Rauma, Finland

Mikko Lauri, Risto Ritala
Department of Automation Science and Engineering
Tampere University of Technology
P.O. Box 692, FI-33101 Tampere, Finland

Atef Z. Elsherbeni
Department of Electrical Engineering
University of Mississippi
University, MS 38677-1848, USA

ABSTRACT

Accurate knowledge of an RFID IC's input impedance enables the design of performance-optimized RFID tags with a given IC. For this purpose, the most valuable information is the IC's input impedance at its wake-up power, but as the impedance itself is power-dependent, few simple methods exist to extract this information. This paper presents a method, based on the joint use of computational electromagnetics, wireless RFID tag measurements and Monte Carlo simulations, to determine the input impedance of an UHF RFID tag chip at the wake-up power of the IC and the measurement uncertainty related to the result.

Keywords: Impedance measurement, microwave measurements, non-invasive, RFID IC, UHF RFID.

1. Introduction

Radio frequency identification (RFID) is based on electromagnetic interaction between a reader and electronic labels, commonly referred to as tags. In this article, we concentrate on UHF RFID systems, where the interaction mechanism is wave propagation within frequencies from 865 MHz to 955 MHz, depending on local radio regulations.

In this type of RFID system, the tags are antennas, loaded with an integrated circuit (IC) and the tag-to-reader communication is based on modulation of antenna scattering by switching the input impedance of the IC. Most commonly, the tags are not equipped with a power source (passive tags), but they scavenge energy from the carrier tone of the reader to power up the IC. This way, very low manufacturing costs per tag can be achieved.

As the operation of passive RFID tags is based on power harvesting, good impedance matching between the tag antenna and the IC is crucial for the operation range of a passive RFID system. To maximize the power delivery to the IC, the tag antenna needs to be conjugate-matched to the input impedance of the IC, but in practice this is challenging, since both the tag antenna and the IC impedances are complex and frequency-dependent and the input impedance of the IC is also power-dependent [1-2]. Furthermore, the mounting parasitics affect the input impedance of the IC.

Manufacturers' datasheets typically list the input impedance of RFID ICs at a few frequency points within the intended operation frequencies or present an equivalent circuit model without showing the actual measurement data. Thus, by measuring the input impedance of the mounted IC so that the contribution of the process-specific mounting parasitic is also accounted for, the uncertainty related to the conjugate matching can be reduced significantly.

Existing methods for measuring the input impedance of an RFID IC employ an RFID tester to find the minimum output power required to active the IC and a vector network analyzer (VNA) for measuring the input impedance of the IC [3]. This way the measurement is conducted at the sensitivity level of the IC, but as the input impedance of the IC is capacitive and varies significantly from the typical 50−Ω characteristic impedance, controlling the uncertainty of the measurement may be problematic, since the sensitivity of the VNA is best around the characteristic impedance with performance decaying rapidly with loads differing from it [4]. This can be alleviated by using static pre-matching. Furthermore, the mounting parasitics can be

accounted for by mounting the IC under test in the same manner as it will be mounted on the tags.

In this article, we propose a wireless method for measuring the input impedance of an IC mounted on an RFID tag. Tag antennas with simulated electrical characteristics will be used as test beds for recording the transmitted power corresponding to the wake-up power of the tag IC versus frequency. The proposed method includes few specialized measurement devices.

2. Theoretical Foundation

Power transfer between complex source (tag antenna) and load (tag IC) impedances, $Z_{tag} = R_{tag} + jX_{tag}$ and $Z_{IC} = R_{IC} + jX_{IC}$, respectively, can be evaluated in terms of the power transmission coefficient (τ), defined as the ratio of the accepted power to the load (P_{IC}) and the available power to the load (P_{tag}). Using an equivalent circuit model, the power transmission coefficient is then expressed as [5]

$$\tau = \frac{4R_{tag}R_{IC}}{\left|Z_{tag} + Z_{IC}\right|^2}. \quad (1)$$

In an anechoic chamber, the wireless channel between the transmitter antenna and the tag can be approximated by the Friis' model. In the present study, we use linearly polarized transmitter antenna and tag antennas, carefully aligned to minimize the link loss due to polarization mismatch. In this case, under the Friis' formulation [6], the accepted power to the IC is

$$P_{IC} = \tau L_C G_{tag} G_{TX} \left(\frac{\lambda}{4\pi d}\right)^2 P_{TX}, \quad (2)$$

where L_C is the cable loss factor, G_{TX} and G are the gains of the transmitter antenna and the tag antenna, respectively, P_{TX} is the time-average transmitted carrier power, d is the distance between transmitter antenna and the tag under test and τ is the power transmission coefficient between the tag antenna and the IC.

Solving the transmitted power from equation (2) and setting the accepted power to the IC to be equal to the sensitivity of the IC ($P_{IC,0}$), we define the transmitted threshold power as

$$P_{TH} = \frac{P_{IC,0}}{\tau L_C G_{tag} G_{TX} \left(\frac{\lambda}{4\pi d}\right)^2}. \quad (3)$$

In this study, the threshold power measurements were conducted in a compact anechoic cabinet and in order to suppress the possible effects of multipath propagation due to non-idealities of the measurement environment, we have mapped the measured threshold power to its value in empty space by using a correction factor Λ, which is the ratio of the measured link loss from the generator output to the input of a hypothetic isotropic radiator placed at the tag's location. In our measurements, the factor Λ is determined by a calibration procedure of the measurement system used.

Commonly, the sensitivity of the IC refers to its read sensitivity, i.e. to the minimum power required to reply to the EPC Gen2 protocol's *query* command. This is the most common and expectedly the least power consuming task for the IC, since the tag's reply to *query* consists only of its ID number. Therefore we adopt this definition for the IC's sensitivity as well. Consequently, as we measure the impedance at the read sensitivity of the IC, the measurement result is useful for designing RFID tags with maximal readable range, but this may not yield maximal operation range for other commands, such as *write*.

To solve the IC impedance based on the measured threshold power, we first rearrange equation (1) to the following form

$$4R_{tag}^2 \frac{1-\tau}{\tau^2} = \left(R_{IC} - R_{tag}\frac{2-\tau}{\tau}\right)^2 + \left(X_{IC} - \left(-X_{tag}\right)\right)^2, \quad (4)$$

which defines a constant-τ circle $C(\tau)$ in the IC impedance plane. The IC impedance is implicitly contained in τ, which is determined from equation (2) by measuring the threshold power of a tag under test.

A single constant-τ circle defines an infinite number of possible impedance solutions, but repeating the measurement of threshold power for two different tags, serving as test beds for the IC of interest, yields two circles and the intersection points of these circles are the possible solutions for the IC impedance. As non-identical circles may intersect with each other at zero, one or two points, care must be taken to pick out the physically meaningful solution in case of two intersection points. The case with only one intersection is extremely rare in practice, and therefore we only consider cases with zero or two intersection points. If there are two intersection points, only one is the physical solution and in case the circles do not intersect with each other, the IC impedance cannot be determined, due to measurement uncertainty or errors. To overcome the ambiguity of the impedance solution, we measure three tags to identify the physical solution as described below.

Assuming a sufficiently small measurement uncertainty and small enough difference between the individual ICs mounted on three test bed tag antennas, the physical solutions from each tag pair are expected to be close to each other – ideally at the same point – in the complex

plane, as illustrated in Fig. 1. To identify these solutions, we consider the triplets of the solutions (circle intersection points marked in Fig. 1), where only one solution produced by each tag pair is included.

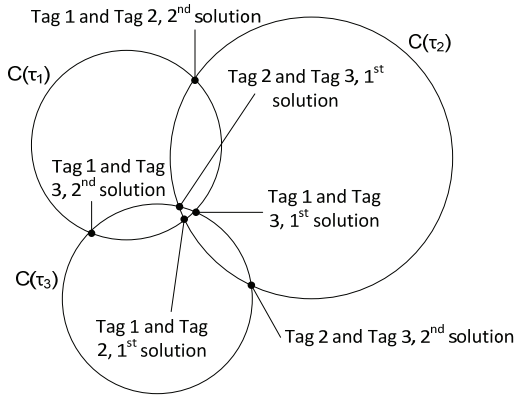

Figure 1 - Illustration of three intersecting constant-τ circles. Intersection points are the possible solutions for the IC impedance.

As we know that ideally the triangle spanned by the physical solutions would degenerate to a single point, we expect this triplet to be formed by the three solutions spanning a triangle with the minimal circumference in the complex plane. Referring to the example in Fig. 1, this triplet would be formed by the first solutions from each measured tag pair.

3. Experimental Verification

To verify the proposed method, three test bed tags referred to as Tag A, Tag B and Tag C were fabricated. There are only few requirements for these antennas. Firstly tag antenna gain and power matching with the IC need to be sufficient over the frequencies of interest to allow the threshold measurement. Secondly, the antennas need to be slightly non-identical, since for identical antennas the circles in Fig. 1 would, in theory, lie on top of each other and the intersection point method described to determine the IC impedance would not be justified. In practice, the fabrication tolerances and measurement uncertainties may provide the required difference, but in accordance with the theoretical foundations presented in Section 2, we use distinct test bed tag antennas to verify the method. Lastly, as the input impedance obtained by the proposed method is the input impedance of the whole circuitry beyond the antenna terminals (IC with its mounting straps), it is crucial to incorporate an identical antenna-IC connection in the test bed tags as in the designs where the measured IC impedance is to be applied.

In this study, we have chosen to characterize the electrical properties of the test bed tag antennas by simulations, but measured characteristics could be used as well. In order to reduce geometry-based modeling uncertainties we chose to use simplistic straight dipole antennas, but in general there are no restrictions for the shape of these antennas. The lengths of the antennas were chosen so that they operate in between their first and second resonance, where the antenna impedance is inductive. This provides sufficient power matching to the capacitive IC under test to allow the threshold measurement. The shape and dimensions of the test bed tag antennas are described in Fig. 2.

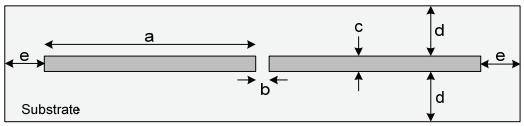

	a [mm]	b [mm]	c [mm]	D [mm]	e [mm]
Tag A	74.5	1	3	15	15
Tag B	79.5	1	3	15	15
Tag C	84.5	1	3	15	15

Figure 2 - Geometry and the related dimensional parameters of the test bed tag antennas.

The assembled tags are equipped with the Alien Higgs-3 IC [7], which is provided by the manufacturer in a strap for easy attachment. Conductive epoxy was used to attach the strap to the antenna. Substrate material used for all fabricated tag antennas is 3 mm thick Rogers 5880, with 35 μm copper cladding, a relative permittivity of 2.2 and a loss tangent of 0.009.

Two different numerical techniques were used to simulate the electrical properties of the test bed tag antennas; FEM-based Ansoft Corporation's High Frequency Structure Simulator (HFSS) and a finite-difference time-domain (FDTD) code based on [9]. Simulated antenna impedance and gain in the direction normal to the antenna plane and away from the substrate for all test bed tags are shown in Figs. 3 and 4, respectively.

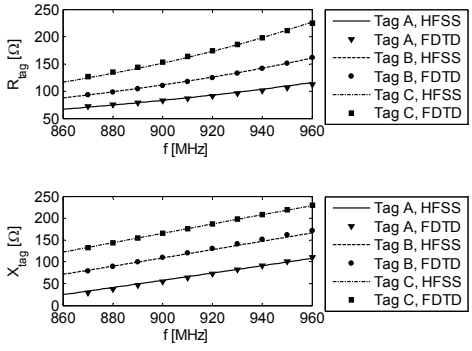

Figure 3 – Simulated impedance of the test bed tag antennas.

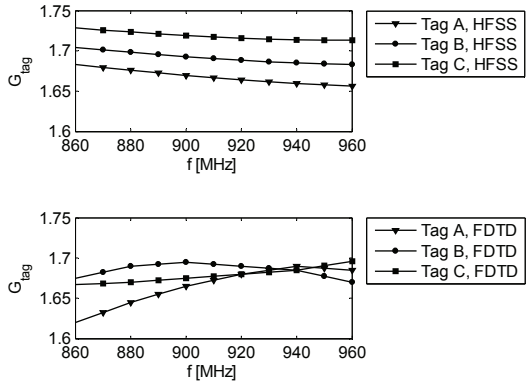

Figure 4 – Simulated gain of the test bed tag antennas referred to an isotropic radiator.

The only difference between the test bed tags is the antenna length (the dimensional parameter *a* in Fig. 2), and thus they all have similar frequency responses. At each frequency, both simulators predict an increase in resistance and reactance versus the antenna length. Based on HFSS simulation, the tag antenna gain shows similar behavior versus the antenna length, but at some frequencies the FDTD results do not follow this trend. Nonetheless, the difference between all the simulated quantities with the two different numerical techniques is less than 5% over the frequencies of interest. This provides additional assurance for our simulation procedures and the slightly different results from the two simulators serve as an example of how small uncertainty in the simulated parameters affect the final outcome of the method.

4. IC Impedance and Measurement Uncertainty

The threshold power of the test bed tags was measured in a compact anechoic cabinet with Tagformance measurement device [9], which is a measurement unit for RFID tag performance characterization. It allows power ramping at a defined frequency and thereby threshold power analysis. The core operations of the device are performed with vector signal analyzer. Sample mean of five threshold measurement on each test bed tag, including the path loss correction are plotted in Fig. 5 with the left hand side y-axis. The maximum gain of the transmitter antenna, provided by the manufacturer, is shown in the same figure with the right hand side y-axis. In the measurement, the separation between the transmitter antenna and the tag under test was 0.45m and the maximum gain of the transmitter antenna was aligned towards the direction of simulated maximum gain of the tag under test.

The threshold curves in Fig. 5 contain information on the gain and impedance matching of the test bed tag antennas. These both affect the power delivery from the incident wave to the IC. For example, for Tag B the minimum measured threshold power is $P_{TH} \approx 1.2$ dBm around 900 MHz. At this frequency the free space attenuation factor $(\Lambda/4\pi d)^2$ under the Friis' model is approximately −24.7 dB. According to Fig. 4, at the same frequency the simulated gain of Tag B is approximately 1.7 (2.3 dBi) and the transmitter antenna gain is 7.2 (8.6 dBi). Summing these values shows that around −12.6 dBm incident power on the IC enables the tag to response to *query*. Since the read sensitivity of the IC is −18 dBm [7], there is an around 5.4 dB mismatch loss, which translates to a power transmission coefficient $\tau \approx 0.29$. Thus, the impedance matching of the bed tags is only modest, yet sufficient to allow the threshold power measurement through the frequencies of interest. This highlights the fact only a very crude initial guess of the IC impedance is needed for the usage of the proposed measurement method. It can also be seen from Fig. 5 that despite the modest power matching observed, the highest transmitted power needed in the experiment was only 5 dBm. This suggests that the measurement method is suitable for larger chambers as well.

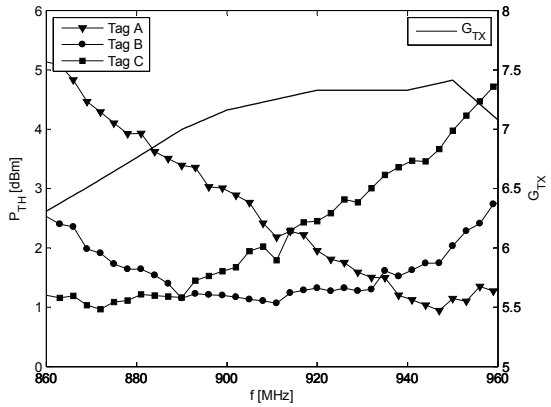

Figure 5 – Measured threshold power of the test bed tags and the gain of the transmitter antenna referred to an isotropic radiator.

We have applied Monte Carlo simulation methods to determine the IC impedance and to quantify its uncertainty. In order to perform the simulations, we first estimate the probability distribution function (pdf) for the tag antenna impedance Z_{tag}, gain G_{tag} and threshold power P_{TH}. As shown by measurements in [3], the read sensitivity of ICs is nearly constant over

bandwidth of interest and thus we take it to be constant in our simulations.

Based on the principle of maximum entropy [10], we have chosen to represent the four quantities of interest as a vector valued random variable $\mathbf{x} = [R_{tag}, X_{tag}, G_{tag}, P_{TH}]$, following a multivariate normal distribution $N(\mathbf{x}; \boldsymbol{\mu}, \boldsymbol{\Sigma})$ with parameters $\boldsymbol{\mu}$ and $\boldsymbol{\Sigma}$, the mean vector and covariance matrix, respectively. Mats et al. [11] studied the impedances of certain commercial tag antenna designs and found the 95% confidence limits of the real part of the impedances to be within ±10 percentage points of their mean value but also less than 3 Ω even for antennas with a high resistive impedance and the 95% confidence limits of the imaginary part of the impedance to be at approximately 3% of their mean value. Additionally, they report that there is a slight positive correlation between the real and imaginary parts of the impedance.

Based on [11], a standard deviation of 3% proportional to the mean value is set for both the real and imaginary part of the tag antenna impedance in our test bed tags, with an additional limitation that the standard deviation is not allowed to be lower than 0.5 Ω or higher than 10 Ω. A weak linear correlation coefficient of 0.25 between the real and imaginary part is assumed. Additionally, based on authors' experience, the tag antenna gain is assumed to have a proportional standard deviation of 2% of its mean value on linear scale. The standard deviation for threshold power is obtained through a standard procedure [12] as sample standard deviation from measured data. It is different for each of the tags and frequencies measured, with typical values of standard deviation ranging from 1% to 2% of the sample mean of the measurement result. For each of the k tags measured, we now have frequency dependent parametric pdf estimates $N(\mathbf{x}_k; \boldsymbol{\mu}_k(f), \boldsymbol{\Sigma}_k(f))$.

On each measured frequency we draw a random sample from the k parametric pdf estimates and compute for each possible pair of tags the sample means of the IC impedance, which give the expected value and the sample covariance matrices quantifying the uncertainty associated with the expected values. A method described in Section 2, Fig. 1 involving a search through all possible solution triplets to identify the physical solution as the triplet spanning a triangle with the minimal circumference in the complex plane is applied to the sample means. With this procedure we have estimated the parameters of three conditional probability distributions of the IC impedance $f_i(Z_{IC}|\mathrm{Y_i})$, where $\mathrm{Y_i}$ are the data sets containing all measurement and simulation data related to the most probable solution triplet in Fig. 1. We approximate the three distributions as independent and apply Bayes' formula [10] to obtain an estimate $g(Z_{IC}|\mathrm{Y_1},\mathrm{Y_2},\mathrm{Y_3})$ of the distribution of the IC impedance given all data sets $\mathrm{Y_i}$. Since all $f_i(Z_{IC}|\mathrm{Y_i})$ are normal distributions with parameters $\boldsymbol{\mu}_i$ and $\boldsymbol{\Sigma}_\mathrm{i}$, $g(Z_{IC}|\mathrm{Y_1},\mathrm{Y_2},\mathrm{Y_3})$ is also a normal distribution with parameters $\boldsymbol{\mu}_t$ and $\boldsymbol{\Sigma}_\mathrm{t}$ given by

$$\boldsymbol{\Sigma}_t^{-1} = \boldsymbol{\Sigma}_1^{-1} + \boldsymbol{\Sigma}_2^{-1} + \boldsymbol{\Sigma}_3^{-1} \tag{7}$$

$$\boldsymbol{\mu}_t = \boldsymbol{\Sigma}_t\left(\boldsymbol{\Sigma}_1^{-1}\boldsymbol{\mu}_1 + \boldsymbol{\Sigma}_2^{-1}\boldsymbol{\mu}_2 + \boldsymbol{\Sigma}_3^{-1}\boldsymbol{\mu}_3\right), \tag{8}$$

where $(\cdot)^{-1}$ denotes matrix inversion. Figures 6 and 7 show the final estimates with one standard deviation limits for the resistance and reactance of the IC under test using both HFSS and FDTD simulation data. The means are indicated by opaque markers and the one standard deviation limits are represented by the bars. The mean values are obtained from equation (8) and the standard deviations from equation (7).

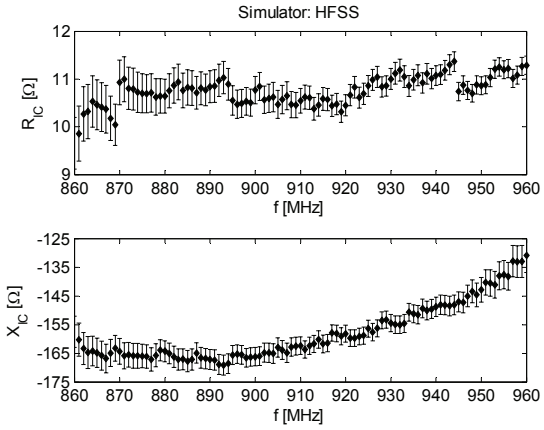

Figure 6 – Real and imaginary part of the IC's input impedance with one standard deviation bars using HFSS simulation data.

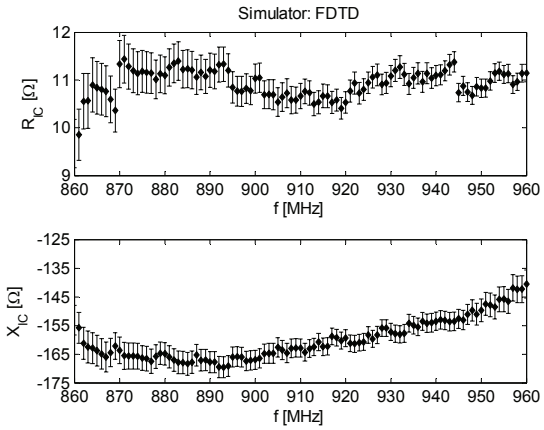

Figure 7 – Real and imaginary part of the IC's input impedance with one standard deviation bars using FDTD simulation data.

Compared with the FDTD data, the final results with HFSS simulation data show a steeper rise trend in the reactance after 920 MHz, but both methods predict the dip in reactance around 890 MHz. The standard deviations depict the uncertainty in the impedance and they are nearly equal using either simulation data. This suggests that the reliability of the proposed measurement method does not depend on selection of the simulation tool, as long as the accuracy of the solver is sufficient and the simulation model includes the essential physical details. The results obtained are credible from the physical point of view and indicate that our method is feasible for studying the input impedance of UHF RFID tag chips.

It should be noted that the equivalent circuit model in the manufacturer's datasheet [7] gives somewhat different values for the input impedance of the measured IC. However the measured values are not directly comparable with values from the datasheet's circuit model, since we measured the input impedance at the read sensitivity of the IC, which is −18 dBm and the circuit model is given at −14 dBm input power.

5. Conclusions

We have introduced a wireless measurement method, based on joint use of computational electromagnetics, wireless RFID tag measurements and Monte Carlo simulations, to determine the input impedance of an UHF RFID tag chip at the wake-up power of the IC and the measurement uncertainty related to the result. The method takes into account the IC mounting parasitics and thus provides ready-to-use data for tag antenna designers. We also applied the proposed method to measure the input impedance of a commercial EPC Gen 2 UHF RFID tag chip.

6. REFERENCES

[1] Karthaus, U., Fischer, M., "Fully integrated passive UHF RFID transponder IC with 16.7-μW minimum RF input power", Solid-State Circuits, IEEE Journal of, vol. 38, no. 10, pp. 1602-1608, Oct. 2003.

[2] Loo, C.-H., Elmahgoub, K., Yang, F., Elsherbeni, A. Z., Kajfez, D., Kishk, A. A., Elsherbeni, T., Ukkonen, L., Sydanheimo, L., Kivikoski M., Merilampi, S., Ruuskanen, P., "Chip Impedance Matching for UHF RFID Tag Antenna Design", Progress In Electromagnetics Research, PIER 81, 359-370, 2008.

[3] Nikitin, P. V., Rao, K. V. S., Martinez, R., Lam, S.F., "Sensitivity and Impedance Measurements of UHF RFID Chips", Microwave Theory and Techniques, IEEE Transactions on, vol. 57, no. 5, pp. 1297-1302, May 2009.

[4] Agilent Technologies Inc., "Agilent Impedance Measurement Handbook. A Guide to Measurement Technology and Techniques.", 4th edition, June 2009.

[5] Dobkin, D., The RF in RFID: Passive UHF RFID in Practice, Newline, 2008.

[6] Friis, H. T., "A Note on a Simple Transmission Formula", Proceedings of the IRE , vol. 34, no. 5, pp. 254- 256, May 1946.

[7] Alien Technology, RFID IC datasheets: http://www.alientechnology.com/tags/rfid_ic.php

[8] Elsherbeni, A. Z., Demir V., The Finite Difference Time Domain Method for Electromagnetics: With MATLAB Simulations, SciTech Publishing, 2009.

[9] Voyantic Ltd.: http://www.voyantic.com/

[10] Bishop, C. M., Pattern Recognition and Machine Learning, Springer, 2006.

[11] Mats, L., Cain, J. T., Mickle, M. H., "Statistical Analysis of Transponder Packaging in UHF RFID Systems", Electronics Packaging and Manufacturing, IEEE Transactions, vol. 32, no. 2, pp. 97-105, April 2009.

[12] ISO GUM 95 with minor corrections, JCGM 100:2008 - Evaluation of measurement data – Guide to the expression of uncertainty in measurement. BIPM, IEC, IFCC, ILAC, ISO, IUPAC, IUPAP and OIML. 2008.

ASSESSMENT OF EMI AND EMC MEASUREMENTS AND CALIBRATION PROCEDURES AT THE NATIONAL INSTITUTE OF STANDARDS AND TECHNOLOGY[†]

Lorant A. Muth and Dennis Camell
Electromagnetics Division
National Institute of Standards and Technology
Boulder, CO 80305-3328

Abstract

We report on the initial phase of our study to assess the electromagnetic interference and electromagnetic compatibility measurement and calibration procedures at the National Institute of Standards and Technology. We are developing a measurement-based uncertainty analysis of calibrations and measurements in the anechoic chamber. We intend to characterize all sources of uncertainty, which include *power and probe-response measurements, noise, nonlinearity, polarization effects, multiple reflections in the chamber, drift, and probe-position and probe-orientation errors.* We present simple and repeatable measurement procedures that can be used to determine each individual source of uncertainty, which then are combined by means of root-sum-squares to state the overall measurement or calibration uncertainty in the anechoic chamber. We report on work in progress and future plans to characterize other EMI/EMC facilities at NIST.

Keywords: calibration, EMI, EMC, measurement, power, probe, uncertainties

1. Introduction

The Electromagnetic Interference (EMI) and Electromagnetic Compatibility (EMC) program at NIST provides customers with measurements performed in anechoic and reverberation chambers, in TEM cells, and on an open area test site (OATS). We have embarked on a program of measurement assessment and are engaged, as a first step, in revisiting the uncertainties that characterize these measurements. We intend to develop for each test site measurement-based uncertainty procedures and tables modeled on the uncertainty analysis procedures recently adopted by the radar cross section community [1]. Specifically, we will determine the uncertainties due to drift or fluctuations in the transmitted power and probe response, inaccuracies in probe position and orientation, multiple reflections, cross-polarization and noise. As a final step, the overall uncertainty of the measurement system will allow us to state the uncertainty in the calibration curve of a probe under test. The specific details of uncertainty tables will vary somewhat from one test site to another, but overall, we aim to develop easily adaptable comprehensive procedures applicable to all test sites at NIST and elsewhere.

Following the format well-established by the radar cross section community, we present an uncertainty table that lists the major component uncertainties in EMC/EMI measurement. If necessary, each uncertainty component can be supported by lower level uncertainty tables that specify how a major source of uncertainty is determined. For example, the overall uncertainty in power measurements is the result of a number of component uncertainties, such as the uncertainty in the power-meter data, the uncertainty in the waveguide coupling constants, and room reflections. The resultant uncertainty in each table can be formed by means of root-sum-of-squares (RSS). In some cases, a stated source of uncertainty will be deemed negligible, if it can be reasonably argued (assumed) that it does not exceed 0.01 dB. Each uncertainty table is valid only for a given frequency (or frequency range) and a specified range of power levels. In a measurement-based uncertainty analysis we will generally specify the upper bounds of uncertainties, instead of statistical averages and standard deviations. Thus, we state our uncertainties at the 98 % confidence level, *subject to* ongoing monitoring and modification based on comparisons of historical and current data. *This requires that a program to monitor sources of uncertainties at regular time intervals be established.*

In Table 1 we state all known sources of uncertainty in the probe calibration procedures for the NIST anechoic chamber. Additional sources of uncertainty will be incorporated, if they become known. We also state the known values of these uncertainties as determined in past studies at NIST [2,3]. These values might be modified as a result of the current research.

2. The anechoic chamber

Figures 1-3 are photographs of the electronics and the chamber used in our study. Two *isolated power meters* record the incident and reflected powers to determine

Table 1.

EMI/EMC CALIBRATION UNCERTAINTY

Probe: H638A 6 mm #2 at 100 cm
Power Density: 0.3 mW/cm^2
$f = 5$ GHz

Sources of Uncertainty	**dB**
Transmitted Power	
Incident power	
Power sensor	0.13
Coupling constant	0.13
Reflected power	
Power sensor	0.13
Coupling constant	0.13
Incident Power Density	
Gain	0.25
Probe Position	0.17
Frequency	negligible
Probe orientation	0.17
Multiple reflections	0.20
Cross-polarization	
Noise	0.25
Drift	0.25
Overall Uncertainty (RSS)	**0.57**

the power transmitted by the horn. A signal generator feeds the amplifiers to excite the waveguide terminated by a horn. The probe (check standard) used is an electrically short (5 cm) dipole with a Schottky barrier diode. The dc voltage from the detector is applied to a high-input-impedance dc voltmeter by means of a RF filter and a high-resistance carbon-impregnated transmission line terminated at the DVM input with a 20 $M\Omega$ load. The signal generator, the amplifiers, the power and the volt meters are powered by state-of-the-art AC power regenerators that reduce the total harmonic distortion in the sinusoidal AC output to $\approx 0.7\%$, filter noise, and deliver a constant AC output voltage of 120 ± 1 V during extended measurements. We thus minimize AC and RF frequency-dependent fluctuations in the measurement system. The 8 m x 5 m x 5 m shielded chamber uses 60 cm or 90 cm high RF absorbers on all surfaces; along the ceiling, the sprinkler system is covered by additional absorbers. A unique 6-axis positioner [4] is used to align the probe (mounted on fiberglass rods) along the horn boresite.

3. Preliminary studies

To develop a comprehensive uncertainty analysis procedure applicable to calibrations and measurements performed in the NIST anechoic chamber, we first examine the importance of drift by observing the transmitted power P_{tr} and the probe response V over an extended period; for example, 24 and 48 hours. In this experiment we have set the signal generator at -5.0 dBm for the duration of the measurements, and the probe was aligned 100 cm from the horn. In Figures 4 and 5, we show the transmitted power and the probe response as functions of time, and in Figure 6, we show the probe response V vs. the square-root of incident power density S_{inc} obtained over 24 hours. In Figure 7, we plot the fractional changes in successive probe responses and transmittted power measurements. These ratios clearly reveal the magnitude of noise and drift in the measurements to be below -100 dB and -50 dB, respectively. These point-to-point drift data can be treated as a random walk to estimate the overall system drift uncertainty. We plan to do this in the near future.

We also obtained data by varying the output of the signal generator from -30 dBm to -2 dBm in 0.1 dB steps. Each output level was held for 20 sec to record multiple data points, and this sequence of measurements was repeated 10 times. Figure 8 shows the power transmitted during the 10 repetitions as a function of time, and Figure 9 shows the probe response as the function of the square-root of the incident power density reaching the probe. We observe a high degree of repeatability in the 10 data sequences. We again take the ratio of successive probe responses to obtain the noise and the drift present in the data, as shown in Figure 10. The sequence of data points at around -40 dB correspond to the start of the next higher setting of the signal generator. We observe that at higher power levels these ratios decrease, because we have reached amplifier saturation levels.

The calibration curve specifies the probe response V as a function of the power density $S_{inc}(x, y, z, \theta, \phi)$ incident on the probe located at (x, y, z) and is given by an N^{th}-order polynomial (with N and the coefficients α_n obtained with least-squares analysis of the data):

$$V = f(S_{inc}) = \sum_{n=1}^{N} \alpha_n S_{inc}^{\frac{n}{2}}, \quad (1)$$

and

$$S_{inc} = \frac{P_{tr} G^{(nf)}(z)}{z^2}, \quad (2)$$

where z is the separation between the horn and the probe, and $G^{(nf)}(z)$ is the near-field gain [2, 5]. Equation (1) automatically satisfies the physical requirement that $V(0) = 0$.

In Figure 9, we show the probe response as a function of the square-root of the incident power density S_{inc} (large circles) with an 11^{th} order (least-squares) polynomial superimposed on the data (line). We also show the polynomial in eq (1) as a function of S_{inc}. The fit is excellent with a mean RSS residual of 10^{-4}, which is the same order of magnitude as the point-to-point drifts observed throughout the measurements.

The polynomial in eq (1) can be used to estimate uncertainty in power due to uncertainties in the probe position, alignment and possibly room reflections. For small variations δz along the boresite,

$$\delta V = \frac{\partial V}{\partial S_{inc}}|_{z0} \delta S_{inc} = \frac{\partial V}{\partial S_{inc}}|_{z0} \frac{\partial S_{inc}}{\partial z}|_{z0} \delta z. \quad (3)$$

Here the partial derivative with respect to S_{inc} can be obtained from eq (1) analytically. Equation (3) can be used to determine experimentally the power variations that give rise to variations in probe response. We can move the probe to $z_0 + \delta z$ and record $V + \delta V$, then use the first equality to obtain the variation in incident power density δS_{inc}. Alternatively, we can plot the probe response in eq (1) as a function of S_{inc} (see Figure 9, top curve) and graphically determine

$$\delta S_{inc} = S_{2,inc}(V_2) - S_{1,inc}(V_1). \quad (4)$$

If the near-field gain is a known or assumed function of z, then eq (2) and the second equality in eq (3) can be used to obtain analytically the relationship between δV and δP or δz. Alternatively, we can use measurements to validate the theoretical function $G^{(nf)}(z)/z^2$. In similar procedures, we can determine the power uncertainties due to (x, y) probe-position uncertainties. Measurements to determine probe-position effects and to validate the near-field gain function given in eq (2) are under way and will be reported soon.

A small uncertainty due to cross-polarization effects in the anechoic chamber and instrumentation exists. Specifically, cross-polarized signals can originate in the signal generator or can be due to misalignments between the waveguide and horn and/or the horn and probe, and can be also generated by the complex reflecting surfaces of the chamber. A measurement-based upper-bound uncertainty can be easily determined. We repeat the experiment as in Figure 8, but with the probe rotated by 90° to record cross-polarized signals, which are significantly lower than the copolarized probe responses. In fact, the range of the copolarized responses is 3.3 mV – 319.5 mV, and the range of the cross-polarized responses is 0.01 mV – 0.55 mV as the incident power density varies from 0.002 mW/cm^2 – 0.704 mW/cm^2. We choose the maximum of the cross-polarized probe response as the uncertainty bound for the cross-polarimetric uncertainty in the full range of incident power densities, $\delta V_p = \pm 0.55$ mV. This assumes that all of the cross-polarized signals will be 100% rotated and detected by the probe, and guarantees that we indeed have an upper-bound uncertainty of

$$\Delta V_p = 20 \log_{10}(1 \pm \frac{\delta V_p}{V}). \quad (5)$$

The corresponding uncertainty in incident power density, $\delta S_{inc,p}$, can be obtained from the first equality in eq (3). In Figure 11 we show ΔV_p. At signal levels below 50 mV the uncertainty is significant. This, however, is an artifact of our procedure, since we chose to bound the uncertainty with the maximum cross-polarimetric signal over the full range of S_{inc}. To exhibit smaller polarimetric uncertainties at low probe levels, we merely have to restrict the range of S_{inc} to 0 mV – 50 mV, for example, and choose the maximum cross-polarimetric signal in this range as the uncertainty bound.

4. Summary and future efforts

We have taken the initial steps to formulate standard procedures to determine measurement uncertainties in the NIST anechoic chamber. Our approach is to obtain *measurement-based* upper-bounds for each uncertainty listed in Table 1. We have taken *repeated* sets of data for transmitted powers in the -30 dB to -2 dB range, and have shown how these data can be used to obtain the uncertainties due to noise and drift. We have used least-squares analysis to obtain a *calibration curve* for the probe response as a function of the incident power density, and discussed how to transform deviations in probe response to an uncertainty in the transmitted power. We have also shown how to obtain the upper-bound uncertainty in probe response due to cross-polarimetric signals. Similar procedures for determining the effects of (x, y, z) probe-position uncertainties can be easily implemented, and measurements have already been started to complete this part of the program. The near-field gain in eq (2) needs to be verified by comparing measurements at various positions along boresite with the theoretical predictions.

Acknowledgment

The authors greatfully acknowledge Galen Koepke, RF Fields Group, Electromagnetics Division, for useful discussions and suggestions.

References

[1] Wittmann, R. C., Francis, M. H., Muth, L.A., Lewis, R. L., Proposed uncertainty analysis for RCS measurements, Natl. Inst. Stand. Technol. NISTIR 5019, January 1994

[2] Hill, D. A., Kanda, M., Larsen, E. B., Koepke, G. H., Orr, R. D., NIST Technical Note 1335, Generating standard reference electromagnetic fields in the NIST anechoic chamber, 0.2 to 40 GHz, March 1990.

[3] Hill, D. A., Kanda, M., NIST Technical Note 1389, Measurement uncertainty of radiated emissions, March 1997.

[4] Kangiser, G., Camell, D. G., New antenna positioner improves NIST capabilities; Industrial Robot, v. 27, no.1, pp. 34 – 38, January 2000.

[5] Kanda, M., Kawalko, S. F., Near-zone gain of 500 MHz to 2.6 GHz rectangular pyramidal horns, Electromagnetic Compatibility, IEEE Transactions, v. 41, pp. 85 – 92, 1999.

Figure 1. The instrumentation used to generate RF power. Two power meters (top) record the incident and reflected powers. Solid state (left), 20 W (center) and 200 W (right) TWT amplifiers are used below 1 GHz and 1 GHz to 18 GHz, respectively. A power regenerator (bottom) powers all the instruments.

Figure 2. The waveguide with the standard gain horn used to transmit into the anechoic chamber. A dual directional coupler is used to measure power with two isolated power meters.

Figure 3. The 8 x 5 x 5 m^3 shielded anechoic chamber is used to calibrate probes from 500 MHz to 50 GHz.

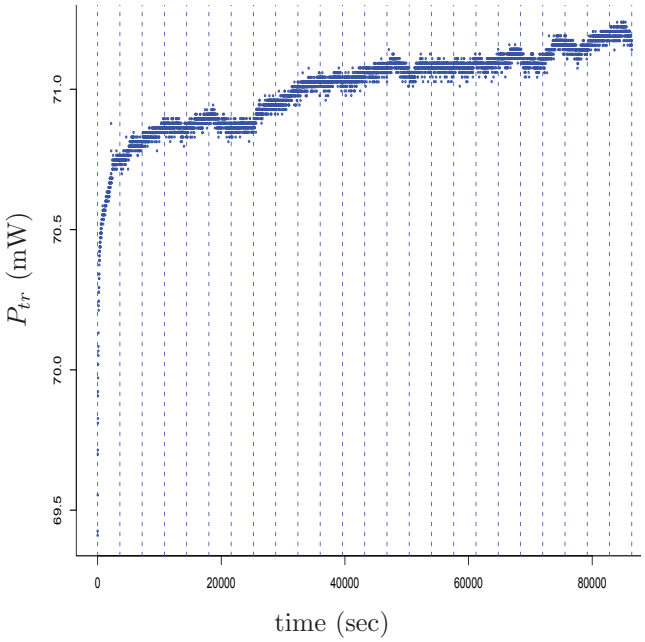

Figure 4. The transmitted power P_{tr} (mW) as a function of time (sec).

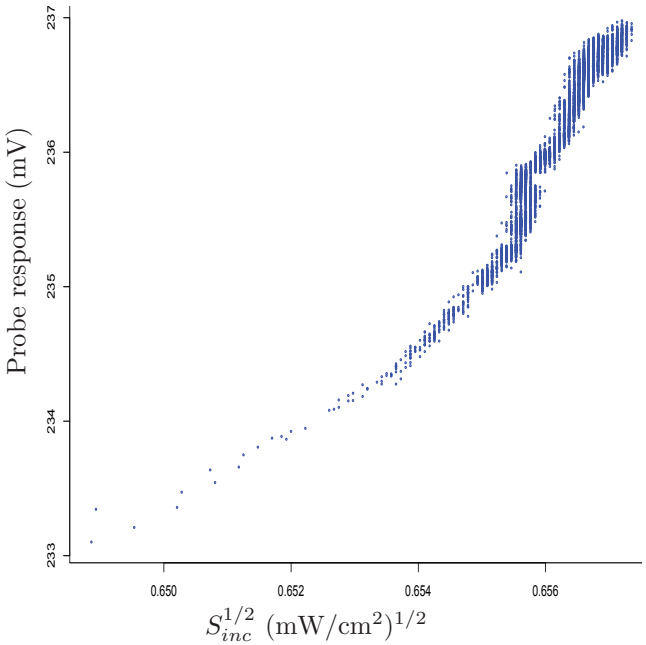

Figure 6. The probe response (mV) as a function of the square root of incident power density (mW/cm^2).

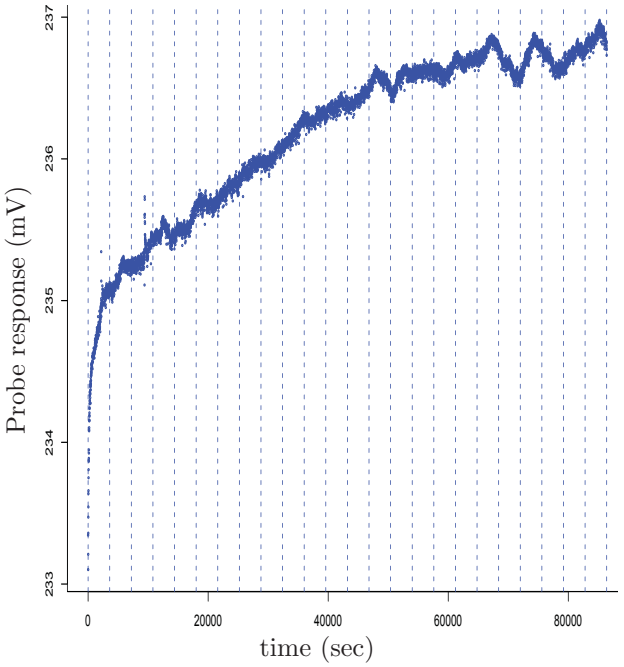

Figure 5. The probe response (mV) as measured with a digital volt meter (mV) as a function of time (sec).

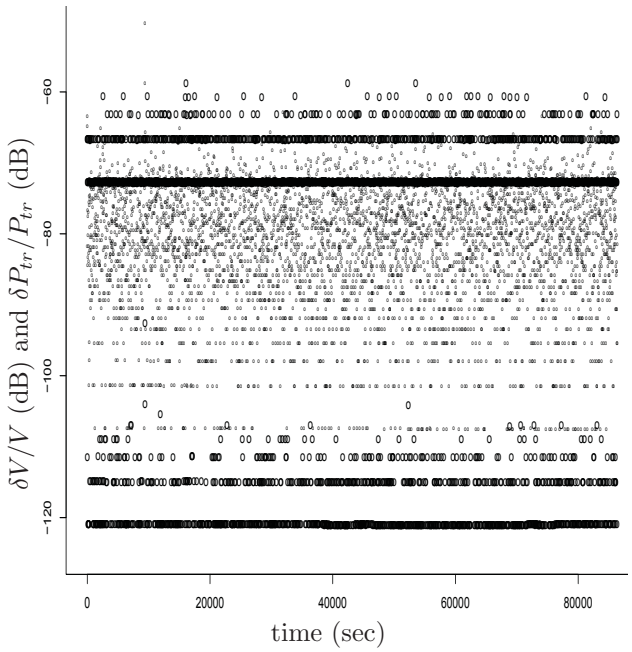

Figure 7. The fractional change (dB) in successive probe responses (small circles) and in successive transmitted powers (large circles).

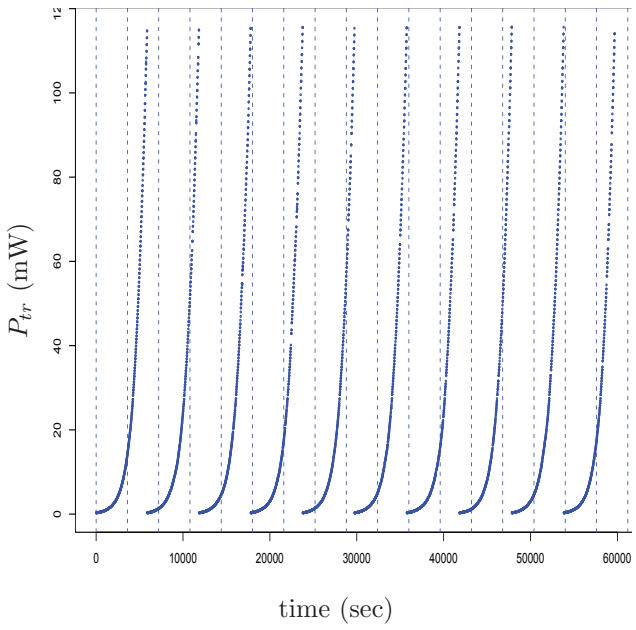

Figure 8. The transmitted power levels (mW) as a function of time (sec).

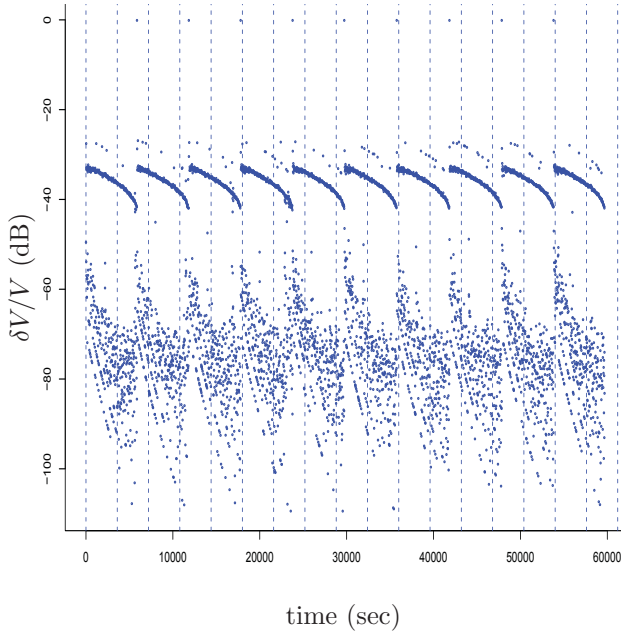

Figure 10. The fractional change (dB) in successive probe responses as a function of time (sec).

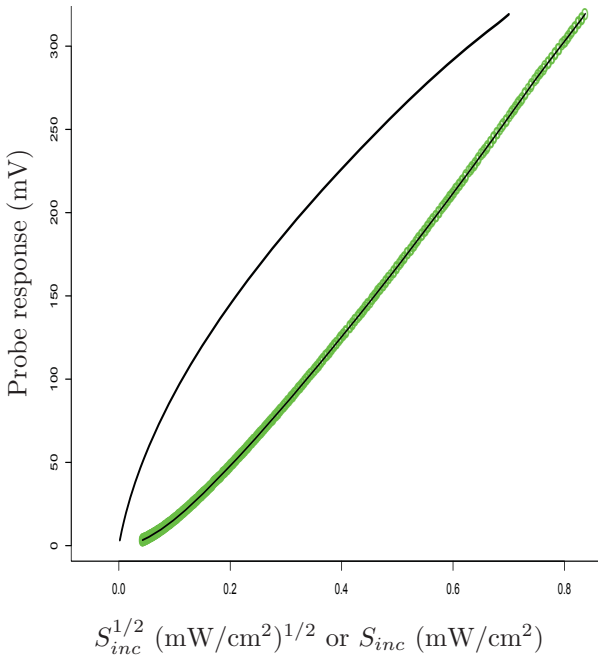

Figure 9. The probe response (mV) (lower curve) with the least-squares polynomial superimposed on the data vs. the squre-root of the incident power density S_{inc} (mW/cm^2), and the least-squares polynomial (upper curve) vs. the incident power density.

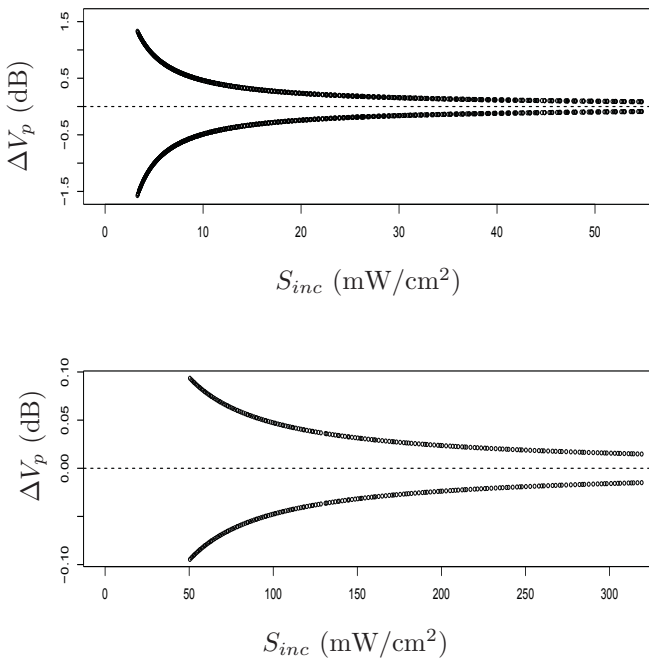

Figure 11. The upper bound of cross-polarimetric uncertainty in the probe response (dB) as a function of the incident power density S_{inc} (mW/cm^2). We have subdivided the incident signal levels for clarity.

EFFECTIVENESS OF LOADING A REVERBERATION CHAMBER – HOW TO CONSISTENTLY LOAD YOUR CHAMBER

Jason B. Coder
University of Colorado
Department of Electrical Engineering
Campus Box 104, P.O. Box 173364
Denver, CO 80217

John M. Ladbury, Christopher L. Holloway and Kate A. Remley
National Institute of Standards and Technology
325 Broadway, Mail Stop 818.02
Boulder, CO 80305

ABSTRACT

In this paper we explore how placing the same amount of RF absorber in different locations within a reverberation chamber can have different loading effects. This difference can have a significant impact on measurement reproducibility, both for measurements in the same chamber and measurements between chambers (i.e., round robin style testing). We begin by discussing some of the theories behind this and show some experimental results from different absorber placements in a reverberation chamber. Our experimental results will be presented in a fundamental format and in a practical sense (RMS-delay spread). We conclude with some suggestions on how to ensure that absorber is placed consistently.

Keywords: Delay Spread, Reverberation Chambers, Wireless Device Testing

1. Introduction

As the use of reverberation chambers expands into experiments and measurements involving loaded setups, there is a need to explore the realistic effectiveness of absorber loading. Significant amounts of absorber are being used routinely in a variety of measurements (for a variety of applications) to lower the Q, decrease the power decay time, and alter the shape of the power delay profile (PDP) [1].

Reverberation chambers are designed to create a consistent test environment with a statistically uniform field throughout the chamber. Many applications have taken advantage of this key principle. For certain applications (i.e., emissions), the original, highly reflective, reverberation chamber is useful. However, newer applications using the reverberation chamber are modifying this environment slightly by loading the chamber with RF absorbing materials. An example of this is the testing of wireless devices [1, 2]. The cell phone industry is beginning to use reverberation chambers for product testing. For this application, the chamber is loaded to simulate a given insertion loss and power decay time that is representative of a real-world communications channel.

Many measurements require the chamber loading to recreate a particular environment. Measurement standards indicate that absorber must be within the working volume, but do not specify exact absorber placement. This raises the questions: Does it matter where in the chamber the absorber is placed? Is there an optimal configuration for the antennas and absorber? These are the questions we hope to address.

These questions are addressed by conducting a series of experiments whereby we measure the relative effectiveness of a fixed quantity of RF absorber placed at different locations within a reverberation chamber. Comparison of measurement results will show the effect of absorber placement within a reverberation chamber.

There are many different parameters we could measure to test our hypothesis. The results could be expressed in terms of power decay time or S-parameters. To keep the results in a general form, we will express them in terms of S-parameters. Recognizing that the wireless device industry commonly refers to parameters in the time domain, we will summarize our results in terms of changes in RMS delay spread.

2. Our Hypothesis and Its Implications

We expect small measureable differences as a result of absorber location in the chamber. Absorber will be placed in a corner (between two walls and a floor), along the wall (between one wall and the floor), in the center of the chamber (sitting on floor) and at various positions elevated off the floor.

The volume inside the chamber, where the average field is statistically uniform, is referred to as the "working

volume." The boundaries of the working volume are defined to be some distance away from any metallic surfaces in the chamber. The IEC 61000-4-21 standard defines this distance as λ/4 from any wall, floor, tuner and/or antenna [3]. Other research indicates that field uniformity begins to diminish within λ/2 of the walls [4]. It is a reasonable assumption that absorber placed within the statistically uniform field of the "working volume" will have a greater loading effect than absorber placed on the floor or next to the walls.

By closely examining the results in [4], we can come up with a reasonable analytical prediction for our hypothesis. Using equations (13), (41) and (64), we should be able to calculate our results for absorber placed on the floor, along the wall, and in the corner, respectively.

Empirically testing our hypothesis can be accomplished by measuring S_{21}, the insertion loss of the chamber. If our predictions are correct, we should see a change in S_{21} as the absorber is moved around the chamber. The fully exposed absorber in the working volume will absorb more energy than that which is only partially exposed near the floor or walls.

When our measurement results are presented, they will be in the form of $<|S_{21}|^2>$. This can easily be expressed in terms of power by use of the following equation from [5]:

$$P_{rec} \propto <|S_{21}|^2> , \quad (1)$$

where the proportionality constant is P_{trans}. Thinking in terms of power, we predict that the amount of received power will depend on placement of absorber. The power transmitted into the chamber will be constant for each measurement, leaving $<|S_{21}|^2>$ as the only variable.

As long as the insertion loss (S_{21}) or similar parameter (power decay time, etc.) is measured before each measurement, any problems with absorber placement can be resolved. We show the outcome of a situation where absorber is moved around after the insertion loss is measured. Absorber might be moved around after the insertion loss measurement to make room for a device under test (DUT) or for easier access to parts of the chamber or antennas.

3. Measurement Setup

All measurements were conducted inside a reverberation chamber consisting of two paddles (one floor to ceiling and one wall to wall). The dimensions of the chamber are approximately 4.2 m long, 3.6 m wide and 2.9 m tall. The two paddles are nearly identical in shape and have a width of 0.7 meters. Figure 1 shows the chamber used in our measurements.

Measurements were conducted by use of a pair of dual-ridged horn antennas (assumed to be identical) mounted on a pair of nonmetallic tripods that are 1.3 m tall. The antennas were connected to a vector network analyzer. Data were acquired at 16,001 discrete points between 800 MHz and 10 GHz and then averaged over 100 discrete paddle steps. When we display our data, we will show results only from 1 GHz to 10 GHz. We discard data below 1 GHz because the antenna mismatch becomes an issue.

The single piece of pyramidal absorber used in these measurements (seen in Figure 1) measures 0.6 m long, 0.6 m wide and 0.6 m tall (to the top of the cones). For the measurements where the absorber is elevated off the floor, styrofoam blocks were used to support the absorber.

Figure 1 – Reverberation chamber used in the measurements with absorber in position 10.

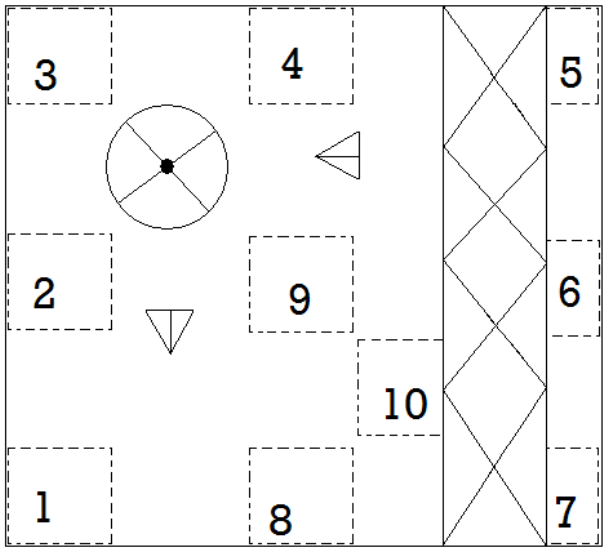

Figure 2 – Locations of absorber (dotted lines) in the chamber. Positions 5, 6, 7 and 10 are partially under the paddle.

To test our hypothesis that proximity to chamber surfaces affects the loading, absorber was placed in ten different locations around the reverberation chamber, and insertion loss (S_{21}) was measured at each location. The diagram in

Figure 2 shows the locations of the absorber in the reverberation chamber. Note that this diagram shows a top down view of the absorber placement.

For positions 1-8, the absorber was placed on the floor of the chamber, against and touching the wall or corner. In positions 2, 4, 6 and 8, the center of the absorber was placed in the center of the wall. While the absorber was at position 9, data were taken while the absorber was on the floor, and again after the absorber was raised to the height of the antennas (approximately 1.3 m). This elevated position is referred to as "9A." In position 10, the absorber was at a height of 0.6 m.

Regardless of the position of the absorber, the antennas remained in the same position and orientation (cross-polarized).

4. Measurement Results and Analysis

At each of the locations shown in Figure 2, S_{21} was measured in phasor form at 100 discrete paddle positions. We computed the squared magnitude of S_{21} at each paddle position, then computed the ensemble average (denoted as < >) to end up with a single $\langle|S_{21}|^2\rangle$ value at each frequency. In addition to this, we measured the insertion loss of the chamber in an empty configuration to use as a reference.

The results of the empty chamber measurement (reference) are shown in Figure 3. Because there is no intentional loading, the losses evident in Figure 3 are due in large part to the wall losses of the chamber. The rippling effect seen at the lower end of the frequency range is due to antenna mismatch. Since the same antennas are used in all of our experiments, any mismatch effects should be constant from measurement to measurement and thus unimportant for our comparisons.

Next, we examined the measurement results for the locations where absorber was placed in the corners of the chamber: positions 1, 3, 5 and 7. In these locations, the absorber should be least effective because it is not fully exposed on three sides. Figure 4 shows data for the four corner locations compared to the reference measurement.

An analysis of Figure 4 shows that each of the four corner absorber positions yields very similar results, so close that the curves are indistinguishable on the plot. To reduce the effects of only sampling at 100 paddle positions, and aid our future analysis, a 101-point moving average is applied to the data. In addition to the moving average, we will compare our results directly to the reference measurement by defining "Absorber effectiveness."This is the difference between the reference insertion loss (unloaded chamber) and the insertion loss measured at the given location. Mathematically, we define absorber effectiveness as

$$A.E. = \langle |S_{21}|^2 \rangle_{ref} - \langle |S_{21}|^2 \rangle_{pos.n} \quad , \qquad (2)$$

where "pos.n" is the given position number.

By calculating A.E. and applying a moving average to the results from positions 1, 3, 5 and 7, we can refine the results of Figure 4 to those of Figure 5. The lowest set of curves shows that a single piece of absorber in any corner of the chamber adds about 5 dB to the insertion loss measurement.

Figure 5 shows that after reducing the rapid variations caused by measuring at 100 paddle positions (by use of a moving average) each corner location shows a consistent amount of absorber effectiveness regardless of which corner it is.

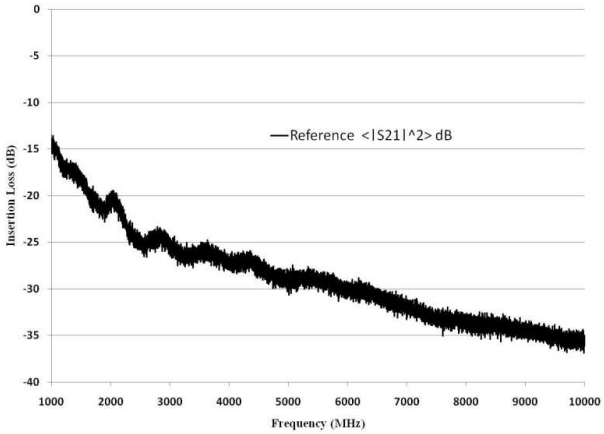

Figure 3 – Reference measurement (no absorber). Insertion loss is shown as $\langle|S_{21}|^2\rangle$ dB.

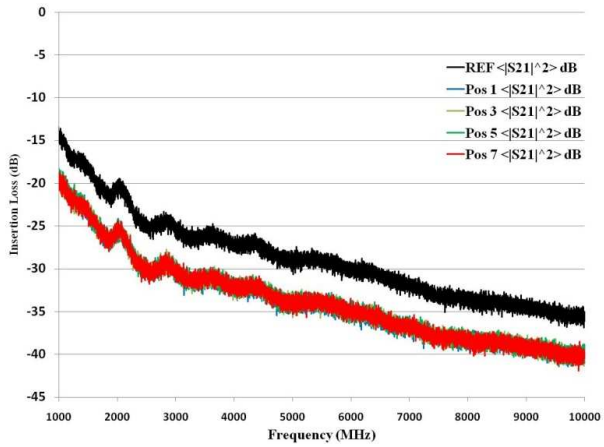

Figure 4 – Measured $\langle|S_{21}|^2\rangle$ dB values for positions 1, 3, 5 and 7 compared to the reference measurement.

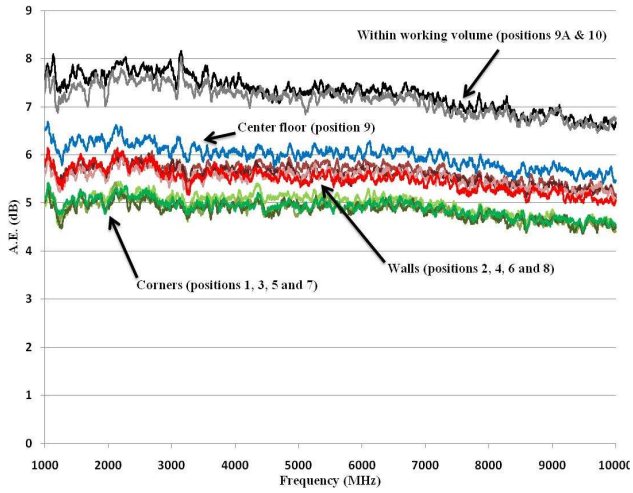

Figure 5 – A summary of the A.E. results.

A similar level of consistency of the corner locations can also be seen in the mid-wall and center positions. The set of curves above the corner positions represent the mid-wall positions (numbers 2, 4, 6 and 8) where only two sides of the absorber are not fully exposed. Absorber in these locations more effectively loads the chamber than the absorber located in the corners of the chamber.

Next, the absorber was placed in the center of the chamber, on the floor. In this location, the absorber has only one side that is not fully exposed. Therefore, we expect increased absorber effectiveness compared to all previous positions. This is reflected in the upper-middle curves of Figure 5.

In addition to testing a single piece of absorber on the floor at position 9, we did an additional test with the absorber elevated to the height of the antennas (1.3 m). At position 9A, the piece of absorber is totally within the working volume of the chamber and should be fully exposed on all sides. At this position, we would expect that the absorber has reached its maximum effectiveness. However, as our hypothesis stated, any absorber placed anywhere in the working volume should provide the same amount of effectiveness. To test this, we placed the piece of absorber at position 10 at a height of 0.6 m above the floor. Figure 6 shows that the results from positions 9A and 10 are nearly identical (to within 0.3 dB).

5. Discussion

Our measurements up to this point seem to coincide with our hypothesis that placing absorber in a corner or against a wall makes it less effective than if it were within the working volume. To more conclusively validate our hypothesis we duplicated the measurements at positions 9A and 10. However, this time we placed a metal plate underneath the absorber. In this configuration, the absorber should be less effective because the metal plate is preventing one side of the absorber from being exposed. We expect our results to look similar to the difference between positions 9 and 9A; placing a plate under the absorber should simulate the piece of absorber sitting on the floor. However, because the size of the plate is much smaller than the size of the floor, we don't expect the results to be identical. Figure 6 shows the original position 9 and 9A results with the addition of the results from position 9A with a metal plate.

Figure 6 shows that when the metal plate is used, results are within 0.5 dB of position 9. The remaining difference between the two configurations is likely due to the fact that the metal plate used was the same size as the bottom of the absorber. When placed on the floor (position 9), the absorber is effectively on a metal plate that is much larger and blocks all energy coming from underneath. With the metal plate, absorber in position 9A can still interact with energy reflected off the floor.

We also placed a metal plate under the absorber in position 10 to show that the result is independent of the absorber location (as long as it is within the working volume). In this configuration, we still expect the result to be close to position 9. Figure 6 shows the original data for positions 9 and 10 with the addition of the results from placing a metal plate under the absorber in position 10.

As with the metal plate in position 9A, use of a metal plate in position 10 yields results that are within 0.5 dB of where we expected to be – equivalent to position 9. The reasoning here is similar; the floor acts as a much larger metal plate than was actually used in positions 9A and 10.

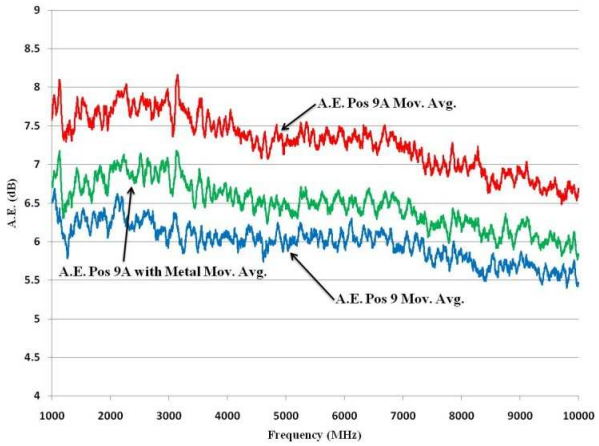

Figure 6 – Comparison between positions 9, 9A and 9A with a metal plate.

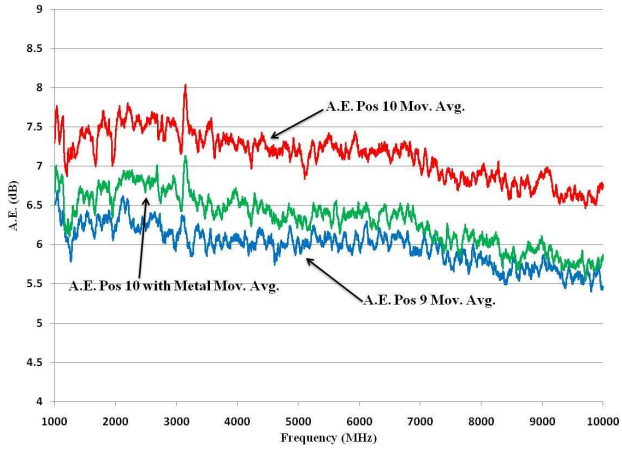

Figure 7 – Comparison between positions 9, 10 and 10 with a metal plate.

6. Effect on RMS Delay Spread and PDP

The link between chamber loading and PDP has been well characterized in [6]. Given this established link, it should follow that the change in chamber loading shown in section 5 should also change the PDP and RMS delay spread. Here, we examine the changes in the RMS delay spread because the changes in PDP should be restricted to changes in slope, not changes in characteristic shape.

The fact that we have very little relative loading for these experiments allows us to approximate our chamber as ideal. This allows for the use of equation (8) from [1], to calculate the RMS delay spread at each absorber position. This equation is given as

$$\tau_{RMS} = \frac{Q}{2\pi f} \quad . \tag{5}$$

Using this equation, we can re-process our measured results to show the RMS delay spread for each absorber position. For simplicity, the results are displayed in terms of a percentage difference from the most effective absorber position, 9A. As an example, the corner positions (least effective) have a RMS delay spread that is between 80 % and 110 % longer than that for absorber placed in position 9A. These results are shown in Figure 8. For reference, the RMS delay spread at position 9A is shown in Figure 9.

The notch near 3 GHz is most likely due to antenna mismatch effects. These effects were present in the A.E. data, but those data are displayed on a dB scale, concealing the effects. Here, on a linear scale, they are more pronounced.

The data shown in Figures 8 and 9 have been averaged to reduce the rapid variations caused by the number of samples taken. This average was employed when Q was calculated, rather than after RMS delay spread was calculated.

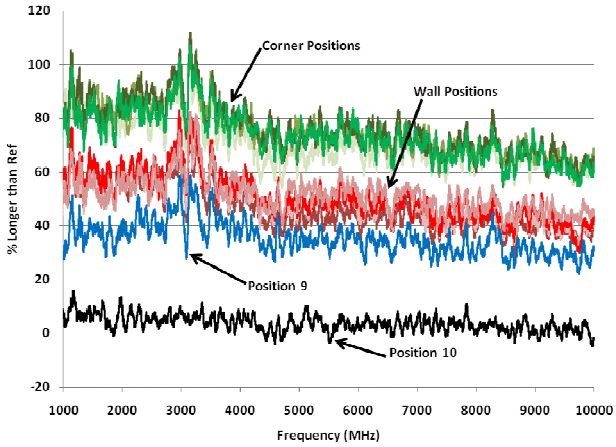

Figure 8 – Percent difference in RMS delay spread compared to position 9A.

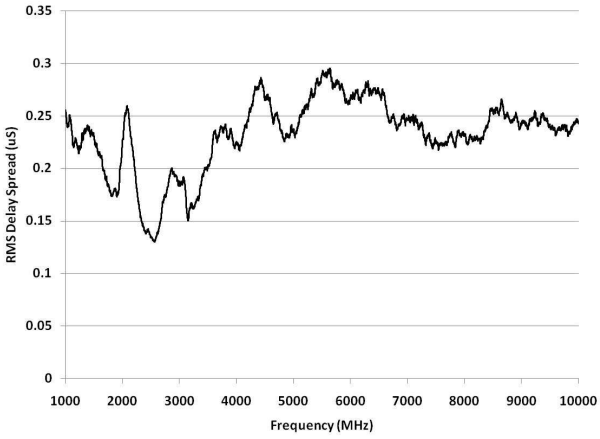

Figure 9 –RMS delay spread of position 9A.

7. Measurement Uncertainties

Uncertainty for these measurements can be estimated after first identifying the contributing factors. The uncertainty from the statistical processing of the measurements is the largest contributor. This initial uncertainty can be reduced through additional averaging, but cannot be eliminated completely. The second factor to be considered is the system drift as the temperature fluctuates throughout the measurement process.

Note that this uncertainty analysis is restricted to those factors that only impact relative measurements. Some uncertainties that would usually affect absolute measurements need not be considered here. For example, uncertainties that manifest themselves as an offset would impact both measurements being considered in (2). Uncertainties of this type would not affect the relative

measurement because they apply to both measurements equally.

The initial statistical uncertainty can be quantified by the standard deviation of the original measurements, before a moving average is applied (i.e., those shown in Figure 4). With no reference measurement subtracted, the data in each absorber configuration have a standard deviation of approximately 0.4 dB. Computing the absorber effectiveness by use of (2) increases this uncertainty by approximately 40 % ($\sqrt{2}$) to 0.6 dB. To reduce this uncertainty we apply a moving average to the data. This will reduce the uncertainty by the following factor:

$$U_{stats} = \frac{0.6}{\sqrt{N_f}} \quad , \qquad (3)$$

where N_f is number of independent frequency samples. This can be determined by calculating the mode bandwidth of the chamber by use of the measured Q of the chamber. In the worst case, our measurements have a bandwidth of about 1 MHz. Given the frequency spacing of our initial measurements and the size of our moving-average window, we have about 50 independent frequency samples in each moving-average window. This results in a final U_{stats} of approximately 0.08 dB.

The second contributor to our final uncertainty number is the result of system drift due largely to temperature (U_{temp}). These measurements were taken over three days (two separate system calibrations). Over this period, the system has an estimated drift of about 0.1 dB.

To compute the cumulative uncertainty (also known as the Combined Standard Uncertainty), we combine these two factors by computing the root-sum-of-squares as shown in [6]:

$$U_{comb} = \sqrt{(U_{stats})^2 + (U_{temp})^2} \quad . \qquad (4)$$

Inserting the terms we determined above, we obtain a combined uncertainty of 0.13 dB. After calculating U_{comb} we can select a coverage factor. We choose a coverage factor of 2, which is common practice [7]. This coverage factor is multiplied with (U_{comb}) to obtain our final measurement uncertainty of 0.26 dB. This value applies to the absorber effectiveness measurements presented here.

Uncertainties for the RMS delay spread calculations will be similar in nature because they are also based on a difference calculation. However, the overall uncertainty will be slightly higher because we approximated our reverberation chamber to be ideal.

Note that the RMS delay spread calculations of the power delay profile are made to show that there is an impact and its approximate magnitude. A more accurate calculation of RMS delay spread can be achieved by calculating the PDP in the time domain, as shown in [6].

8. Conclusions

We have shown that placing a fixed amount of absorber at different locations inside a reverberation chamber can impact the insertion loss and RMS delay spread of the chamber (and thus the "effectiveness" of the absorber). By placing a single piece of absorber at 11 different locations, we showed that as long as all sides of the absorber are fully exposed and within the working volume of the chamber, maximum effectiveness is achieved. Because of this effect, we encourage others to measure the insertion loss of their chamber–in its test configuration–prior to other measurements and to avoid moving the absorber once this measurement has been completed.

8. REFERENCES

[1] E. Genender, C.L. Holloway, K.A. Remley, J.M. Ladbury, G. Koepke, and H. Garbe, "Simulating the Multipath Channel with a Reverberation Chamber: Application to Bit Error Rate Measurements," Accepted for Publication, IEEE Transactions on Electromagnetic Comp., 2010.

[2] C. L. Holloway, D. A. Hill, J.M. Ladbury, P. Wilson, G. Koepke and J. Coder, "On the Use of Reverberation Chambers to Simulate a Rician Radio Environment for the Testing of Wireless Devices," IEEE Transactions on Antennas and Propagation, Vol. 54, No. 11, November, 2006.

[3] IEC 61000-4-21, "Reverberation Chamber Test Methods," International Electrotechnical Commission, 2001.

[4] D. A. Hill, "Boundary Fields in Reverberation Chambers," IEEE Transactions on Electromagnetic Compatibility, Vol. 47, No. 2, pp 281-290, May 2005.

[5] J. Ladbury, G. Koepke and D. Camell, Evaluation of the NASA Langley Research Center mode-stirred chamber facility, National Institue of Standards and Technology, Boulder, CO, 1999, NIST Tech. Note 1508.

[6] X. Chen, P.S. Kildal, "Theoretical Derivation and Measurements of the Relationship between Coherence Bandwidth and RMS Delay Spread in Reverberation Chamber," IEEE European Conference on Antennas and Propagation, 2009, pp 2687-2690.

[7] B. N. Taylor and C. E. Kuyatt, Guidelines for Evaluating and Expressing the Uncertainty of NIST Measurement Results, National Institute of Standards and Technology, Boulder, CO, 1994, NIST Tech. Note 1297.

IMPROVEMENT IN LOW FREQUENCY TEST ZONE PERFORMANCE IN THE BENEFIELD ANECHOIC FACILITY

Lt Christina Jones, James Bartley, Ronnie Fernandez, Michael Shaw
772 TS/EWOI, Bldg 1030 NT, 30 Hoglan Avenue
Edwards AFB, California 93524

ABSTRACT

Anechoic chambers simulate open air test conditions and are advantageous for testing avionics systems in a secure, quiet electromagnetic environment. The 412th Electronic Warfare Group's Benefield Anechoic Facility (BAF), located at Edwards AFB, California was designed for testing systems in the radio frequency (RF) range from 500 MHz to 18 GHz. For frequencies below 500 MHz, the installed radar absorbent material (RAM) does not effectively absorb incident RF energy, thereby allowing undesired RF scattering off the chamber's floor, ceiling, and walls. This leads directly to measurement inaccuracies and uncertainty in test data, which must be quantified for error analysis purposes. In order to meet the desired measurement accuracy goals of antenna pattern and isolation measurement tests below 500 MHz, RF scattering must be mitigated.

BAF personnel developed a test methodology based on hardware gating, range tuning and improved RAM setup, to improve chamber measurement performance down to 100 MHz. Characterizing the chamber using this methodology is essential to understanding test zone performance and thus increases confidence in the data. This paper describes the test methodology used and how the test zone was characterized with resulting data.

Keywords: EM field probing, hardware gating, low frequency range improvement, RAM, range tuning

1.0 Introduction

The Benefield Anechoic Facility, located at Edwards AFB, California was designed for installed avionic and EW system testing in the frequency range of 500 MHz to 18 GHz. Its dimensions of 264 feet in length, 250 feet in width, and 70 feet in height allow it to accommodate large systems under test (SUT) on an 80 foot turntable. The installed 1½ and 2-foot RAM on the floor, ceiling, and walls simulates a free-space environment above 500 MHz. Below 500 MHz, this RAM does not effectively absorb incoming RF energy, allowing undesired scattering off the chamber's floor, ceiling, and walls. This RF scattering, also known as multipath, produces ripple and distortion of the electromagnetic (EM) field in the test zone and contributes to measurement uncertainties, particularly for antenna pattern and isolation measurements. The BAF developed a new methodology and test system for improving chamber performance by mitigating multipath at frequencies between 100 and 500 MHz. This system incorporates three low frequency test assets:

1. Directive source antenna
2. Six-foot RAM
3. Hardware gating system

The 772nd Test Squadron conducted a test from December 2009 to January 2010 using the test system to characterize the chamber and evaluate improvements in the EM environment and measurement accuracy. These improvements were produced by creating a more uniform field in the test zone at frequencies from 100 to 500 MHz.

This paper will discuss the background and baseline test, the test system and methodology, and the test results.

2.0 Background and Baseline Test

RAM RF performance is a function of thickness relative to the wavelength of the RF signal. Because RAM absorption performance decreases as the RF frequency decreases, low frequency measurements in the BAF are limited by the installed RAM. Figure 1 illustrates potential inaccuracies that could occur from the effects of just two signals reflected off the floor and ceiling (multipath).

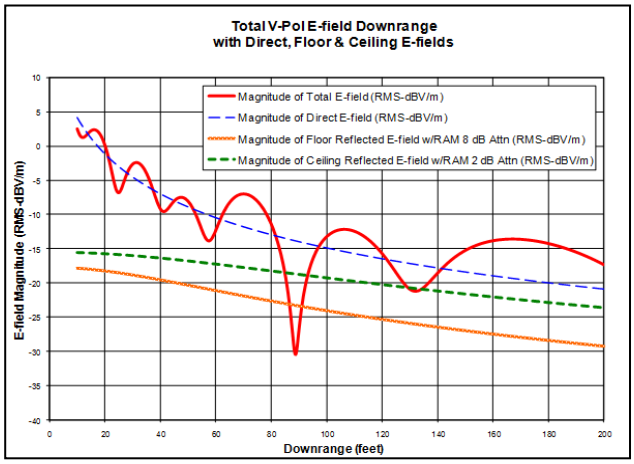

Figure 1: Simulation of Combined E-Field

This analysis was performed at 100 MHz using the setup in figure 2 and shows the effect of the differences in path lengths of the ceiling and floor reflections, the difference

in attenuation due to the RAM on the ceiling and floor, and field strength reduction due to propagation distances. The simulation included 1½-foot RAM on the ceiling and 6-foot RAM on the floor between the transmit antenna and the probe antenna. The result was a downward trend with ripple and distortion compared to the direct E-field. This produced amplitude and phase variations at different locations in the test zone. Variation in the combined E-field is present in the BAF chamber at frequencies below 500 MHz, requiring characterization of the chamber prior to testing.

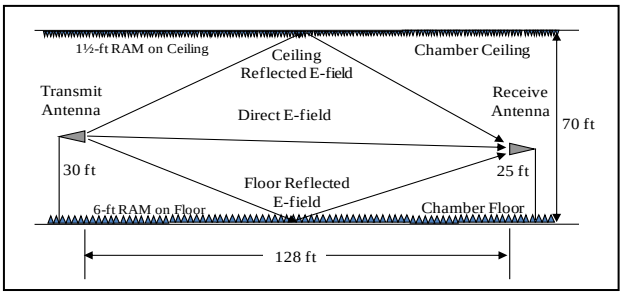

Figure 2: Chamber Setup for Simulation

In 2003, a characterization and performance baseline was conducted to determine chamber performance between the frequencies of 100 MHz and 1 GHz. Measurements were taken across the turntable where majority of tests are located. Crossrange and downrange probing of E-field strength was performed for both vertical and horizontal polarizations at heights of 17 and 30 feet. The RAM layout in the chamber employed 2-foot RAM on the floor and 1½-foot RAM on the ceiling and walls.

The data were evaluated to determine the ripple across a crossrange or downrange probe. The ripple was obtained by taking the difference in decibels (dB) between the maximum and minimum measured power values collected across the one-dimensional probe scan. In vertical polarization, measurements yielded 30 dB of ripple for frequencies below 125 MHz. Above 125 MHz, in vertical polarization, the ripple was measured between 5 and 10 dB. The ripple in horizontal polarization for frequencies between 100 and 300 MHz was 15 dB. Above 300 MHz, the ripple in horizontal polarization was between 5 and 10 dB. The power was measured at only one crossrange and downrange path at two different heights. Consequently, the test zone was sparsely characterized in only two dimensions. During testing, however, it is often necessary to expand the test zone from a two-dimensional test region to a full three-dimensional test volume.

Range tuning was one technique used to reduce the ripple in the test zone. This technique was effective for single frequency testing where the multipath from the primary floor and ceiling reflections co-linear with the source antenna were reduced. The range tuning for one specific frequency resulted in a 2 dB ripple across a small test zone. While this amount of ripple is acceptable for most tests it has the limitation of being effective at one frequency. Tests often require a band of frequencies. Hence the identification of other multipath reduction techniques was necessary to accommodate wider frequency bandwidth test requirements.

3.0 Test System and Methodology

The BAF developed a test system and methodology that improves chamber performance between 100 and 500 MHz. A two-part approach was identified:

1. Reduce the amount of multipath present in the chamber and
2. Reduce or remove the amount of multipath measured at the SUT.

The effects of these two approaches created a nearly uniform field over a limited region known as the ‘quiet zone’ or test zone. To achieve these effects and improve measurement accuracy, the BAF developed a solution by using three components that, when combined effectively, contributed to the significant suppression of multipath effects:

1. Directive source antenna
2. Six-foot RAM
3. Hardware gating system

The Low Frequency Range Improvement (LFRI) test system comprised these components. The first two components reduce the amount of multipath produced in the chamber. Using a more directive source antenna decreased the amplitude of co-linear multipath from the floor and ceiling. Six-foot RAM was utilized in the Fresnel zone to provide better absorption of RF signals at frequencies below 500 MHz. The third component focused on reducing the measured multipath in the test zone. The incorporation of hardware gating effectively eliminated reflected signals from the measurement area, except for those signals which could not be gated out. The combination of these components reduced the effects of multipath on the received signal and improved measurement accuracy.

Cross-Log Periodic Antenna

A TECOM Industries broadband dual polarized log periodic antenna, referred to as the cross-log periodic antenna, was chosen as the directive source antenna. This antenna operates from 30 MHz to 1.1 GHz and has a directivity of 7 dBi. It produces an asymmetrical pattern with a narrow pattern in the E-plane and a dipole shaped pattern in the H-plane. Therefore, the multipath from the floor and ceiling was reduced for vertical but not horizontal polarization. The antenna also provided a 15 dB front-to-back ratio, which reduced reflections from the wall behind the source antenna.

6-Foot RAM

The 6-foot pyramidal RAM, model EPH-72PCL from ETS Lindgren, covered the test range floor between transmit and receive antennas. Manufacturer data shows the 6-foot RAM attenuates RF signals at normal incidence at least 10 dB better than 2-foot RAM at the frequencies between 100 and 500 MHz. An analysis was performed using XGtd®, an EM simulation program by REMCOM, to estimate the improved chamber performance from replacing 2-foot RAM on the floor with 6-foot RAM. The results are shown in figure 3 where the top 20 RF signals are listed and also traced in the 3-D chamber model. The cell highlighted yellow is the RF signal reflected off the floor. After replacing the 2-foot RAM with 6-foot RAM on the floor, this signal's power level dropped 13.5 dB.

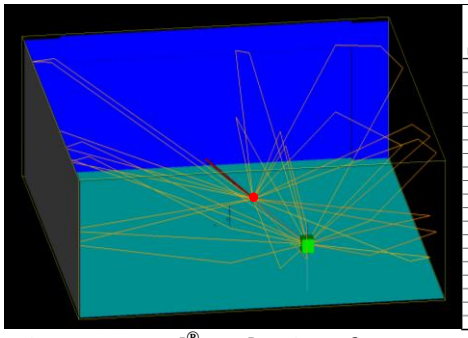

Ray Number	Power Level (dBm) 24" RAM	Power Level (dBm) 72" RAM
1	-40.59	-40.59
2	-48.93	-53.28
3	-53.28	-54.85
4	-54.85	-56.37
5	-55.01	-58.19
6	-56.04	-58.43
7	-56.37	-58.72
8	-57.55	-58.72
9	-58.19	-59.2
10	-58.43	-59.76
11	-58.72	-60.2
12	-58.72	-61.1
13	-59.2	-61.68
14	-59.23	-62.08
15	-59.76	-62.47
16	-59.87	-62.6
17	-60.2	-62.75
18	-61.1	-62.87
19	-61.68	-63.08
20	-62.08	-63.22

Figure 3: XGtd® Evaluation of 6-Foot RAM on Floor

Hardware Gating

Hardware gating was used to gate out undesired chamber reflections. The RF switches in the hardware gating equipment pulsed a continuous wave (CW) signal with an appropriate transmit pulse width (PW) before the signal was transmitted through the source antenna. This technique produced the CW pulse signal. When the desired direct CW pulse signal arrived at the receive antenna, the gate opened briefly to receive it but shut shortly afterward to prevent measuring the unwanted reflections that arrived later. Narrow gates and precise timing between transmit and receive antennas allowed this system to gate out the undesired responses which led to improved measurement accuracy.

Three sub-systems comprised the hardware gating equipment. The Agilent 81104A Pulse Generator was the user interface for setting the gating parameters. It generated the transistor-to-transistor logic (TTL) signals to control the selected PRI, transmit PW, receive gate width, and receive gate delay. The TTL signals from the Pulse Generator drove the states of the high-speed FET absorptive switches in the separate transmit and receive Orbit FR8205 Pulse Modulator Units.

Measurement Equipment

Two different receive probe antennas, a biconical and a dipole, were used to cover the frequency range from 100 to 500 MHz. Antennas with dipole shaped patterns were used to receive signals coming from all directions except at the ends of the antenna. The biconical antenna bandwidth was limited by the ratio between the antenna length and signal wavelength. Consequently, it was used for measurement collection between 100 and 300 MHz. A tuned dipole was used for measurements between 300 and 500 MHz. A chamber coordinate system with the format (x,y) were used during data collection to identify the probe antenna's crossrange and downrange location in relation to position (0,0) at the center of the turntable.

4.0 Test Results

The test objective was to characterize the EM test environment and demonstrate increased measurement accuracy in the test volume at frequencies from 100 to 500 MHz using the test system, with a more concentrated focus between 100 and 300 MHz. The EM test environment and measurement accuracy were quantified by determining how uniform the EM field was over the test volume. The LFRI system diagram is shown in figure 4.

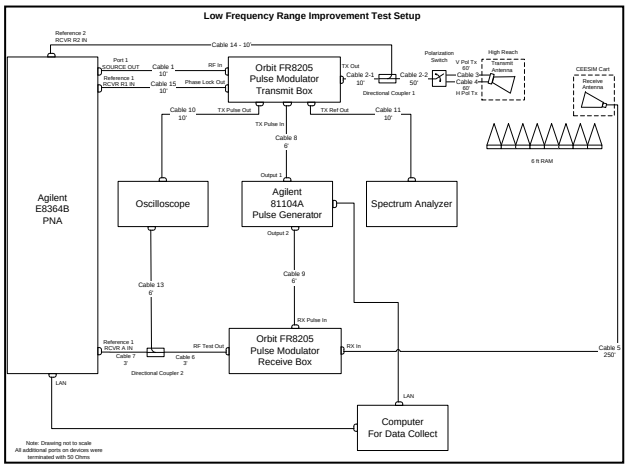

Figure 4: LFRI System Diagram

This test was completed in three phases:

1. Range Tuning
2. Hardware Gating Parameter Optimization
3. EM Field Probing

The results from the first two phases were used to select the test conditions for the third phase.

Range Tuning

In range tuning for frequencies from 100 to 500 MHz, an acceptable test zone was identified by probing 80 feet downrange across the center of the turntable. Figure 5 shows the downrange probe data for vertical and horizontal polarization with nulls circled in red. This data were collected at a crossrange position of zero while the downrange position was varied. Destructive interference between the reflections and the direct signal caused nulls

in the vertically polarized downrange data. In the 100 MHz vertical polarization data, there was a 20 dB null at the positions (0,-7) and (0,37). There was also a large null in the vertical polarization data in 450 MHz at (0,28). The horizontal downrange data did not impact the selection of the test zone since there were no significant nulls in the data. An acceptable downrange location for testing is highlighted in yellow in figure 5.

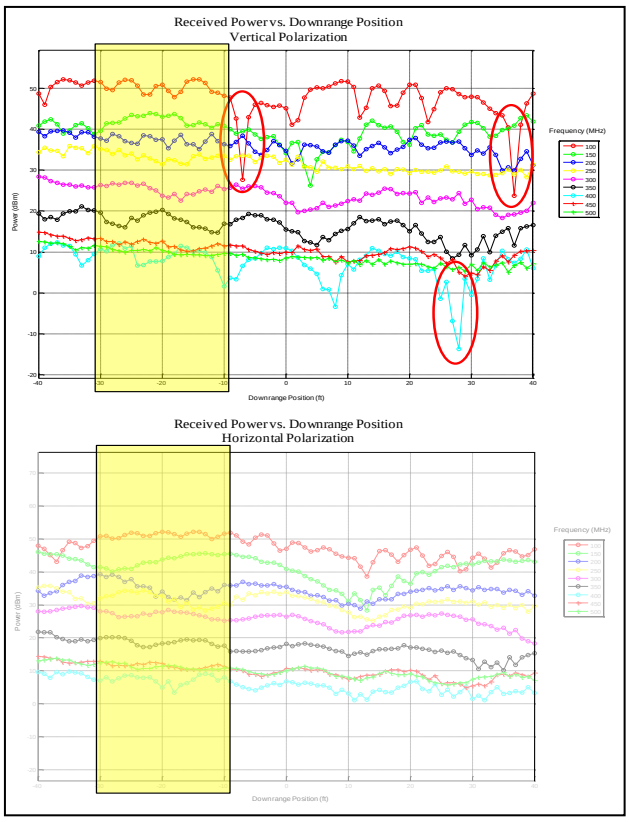

Figure 5: Range Tune Downrange Data

The vertical polarization data had more downrange ripple compared to the horizontal data. This was caused by multiple reflected RF signals adding out-of-phase at the same point spatial location. Figure 5 shows the periodicity of the ripple of the total received power across downrange position. At 400 MHz, the nulls slowly increased with downrange position until a 20 dB null was observed. A similar condition occurred at 100 MHz.

Hardware Gating Parameter Optimization

During the hardware gating parameter optimization phase, the selected hardware gating settings were:

1. PRI = 1 microsecond
2. Transmit PW = 45 nanoseconds
3. Receive Gate Delay = 600 nanoseconds
4. Receive Gate Width = 60 nanoseconds

Initial parameter values were chosen prior to test using mathematical analysis and XGtd® chamber simulation. Downrange and crossrange probing were used to confirm and adjust the parameters chosen before test. First, downrange probe data were analyzed to ensure enough signal strength was present in the transmit PW. Next, the data were evaluated to ensure that both the receive gate delay and receive gate width were sufficient to cover the test volume. Examination of the power levels verified the received power was not rolling-off at the edges of the test volume. Finally, the effect of the PRI on the received data was examined. The PRI needed to be sufficient to produce an unambiguous range so that reflections from one transmitted pulse had dissipated when measurements were collected for the next transmitted pulse. Since a longer PRI resulted in less power received, it was important to select the minimum PRI for an unambiguous range to reduce the amount of conversion loss.

Figure 6 shows the relationship between the hardware gating settings and three locations within the test volume. The receive gate is circled in blue, the transmit pulse is bordered in red, and the arrival of the transmit pulse within the receive gate is highlighted with a bold arrow. At various locations throughout the test volume, the transmitted pulse had to arrive at the receive antenna before the receive gate closed. While 50 nanoseconds was slightly short for an adequate time to receive the pulse in antenna location 3, this value was chosen as a trade-off between a larger receive gate which accepted all the transmitted pulse but also allowed more reflections into the receive gate.

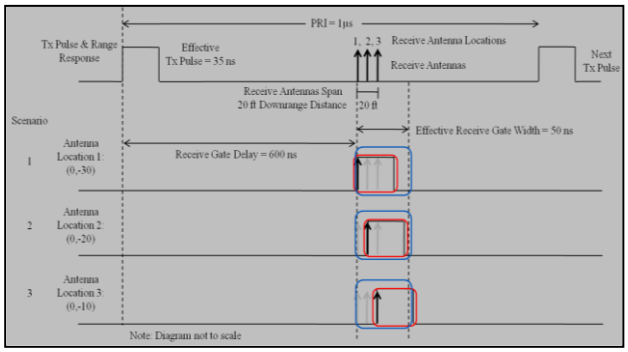

Figure 6: Hardware Gating Settings

EM Field Probing

A biconical antenna and a dipole antenna were used to probe the EM field from 100 to 500 MHz. The test volume was a rectangular cube of 20 feet in length, 20 feet in width, and 13 feet in height. The volume was centered above the (0,-20) position on the turntable, shown in figure 7.

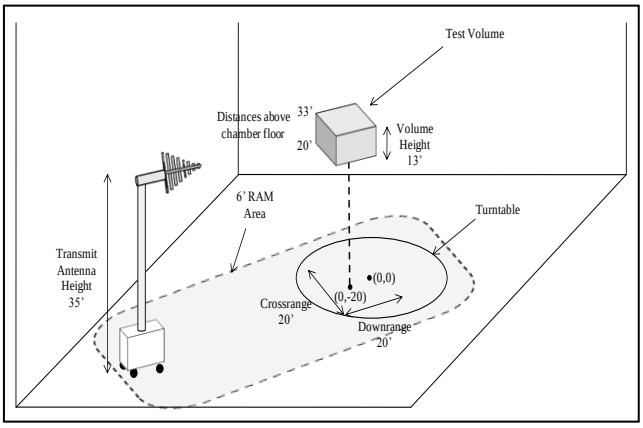

Figure 7: Field Probe Chamber Layout

Two central areas of focus for analysis of the test data in EM probing were:

1. Field uniformity within the test volume, and
2. Efficacy of the hardware gating equipment

Field uniformity throughout the test zone is defined by the flatness of the EM field, which is controlled by the directivity of the source antenna, free space loss due to propagation, and multipath. For this test setup, flatness of the EM field and beam shape taper only minimally impacted the field uniformity. The test zone was in the far field, so the EM field was near planar and the beamwidth of the antenna was large enough to illuminate the entire test volume with less than a dB of amplitude taper. The free space loss across the downrange was estimated to be 1.6 dB and was considered ideal BAF chamber performance. Therefore, this analysis of field uniformity focused on the effect the floor and ceiling multipath had on the test zone. The multipath effect produced ripple across the test zone and is seen in the data collected at 100 MHz in vertical polarization in figure 8. The x and y-axes on the surface plots are downrange and crossrange positions, respectively. The z-axis is the power measured in dB at each position of the slice of data.

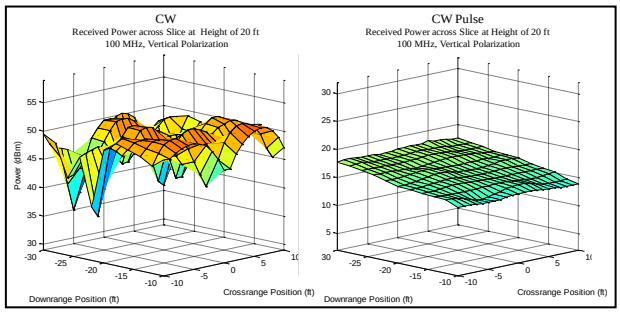

Figure 8: 100 MHz in Vertical Polarization

When the test zone was probed, the ripple effect due to multipath dominated the non-uniformity of the field. This multipath effect is illustrated in the numerous peaks and nulls of the CW data on the left of figure 8. The CW pulse data on the right of figure 8 shows how the hardware gating removed the majority of the peaks and nulls due to multipath. In the CW pulse data, the remaining field non-uniformity was due to the collinear floor and ceiling reflections known as collinear multipath which creates long-wave ripple and downrange reduction of the RF signal due to propagation.

To evaluate the second area of focus, the CW and CW pulse data were compared to show the effectiveness of the hardware gating operation within a slice of the test volume. The minimum received power level was subtracted from the maximum receive power level to quantify ripple for a slice of the test zone. The CW graph showed 16 dB of ripple across the slice of the test volume. The complex interactions between the direct signal and all the reflections caused irregular peaks and nulls across the slice. The CW pulse graph shows approximately 4 dB of ripple across the slice of the test volume. These results demonstrated effectiveness of the hardware gating system removing multipath except for the two collinear reflections off the floor and ceiling.

Figure 9 shows the horizontal data collected at 100 MHz. The plots show how the hardware gating removed the large null and other variations seen throughout the slice of the test volume compared to CW mode. The ripple of the CW data was 23 dB and showed that the variation in power occurred more drastically as the receive probe moved downrange instead of crossrange. The CW pulse data showed 8 dB of ripple. These results illustrated that the hardware gating system was effective in gating out many of the reflections that caused ripple in a test zone.

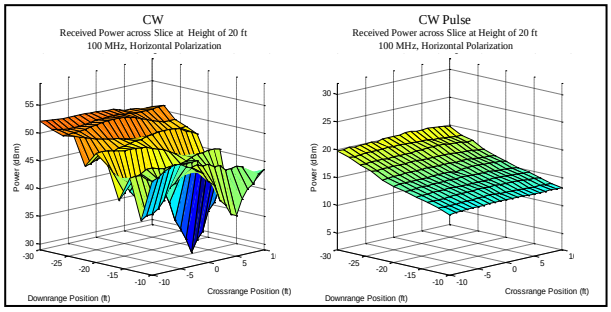

Figure 9: 100 MHz in Horizontal Polarization

Figure 10 summaries the ripple data calculated from the maximum and minimum values across the entire test volume for specific frequencies. For data analysis purposes, the data were color coded to allow quick evaluation of the ripple. The red cells have the largest amount of variation and gray cells have the least.

No taper corrections were applied to normalize the data across the test volume with respect to free space loss due to the complex amplitude and phase interactions of the ceiling and floor reflections with the direct signal.

Probe Antenna	Freq (MHz)	Vertical Polarization		Horizontal Polarization	
		CW	CW Pulse	CW	CW Pulse
Biconical Antenna	100	46.7	8.2	23.0	8.4
	110	24.2	6.9	17.8	8.2
	120	24.9	6.4	18.9	6.1
	130	14.4	4.5	16.1	8.1
	140	16.4	5.8	15.8	7.4
	150	11.7	5.2	14.8	7.8
	160	13.1	5.7	15.8	9.0
	170	16.4	4.5	14.8	8.7
	180	11.5	5.9	14.6	8.1
	190	10.6	4.8	9.2	6.7
	200	8.6	3.8	14.3	8.4
	220	9.6	4.3	10.2	7.2
	240	7.7	3.9	9.0	6.9
	260	9.0	5.1	11.1	7.1
	280	8.7	6.0	10.2	7.0
	300	8.9	6.6	7.7	6.4
Dipole tuned to 375 MHz	320	6.7	4.7	7.2	5.3
	340	4.9	3.6	5.2	4.6
	360	4.8	3.1	5.3	3.9
	380	4.7	3.1	5.7	3.9
	400	3.7	2.4	5.1	3.8
Dipole tuned to 425 MHz	440	3.4	2.2	4.1	2.9
	480	4.4	3.7	4.5	3.3
	500	4.9	3.9	4.5	3.8

Legend

	Δ > 12 dB		6 < Δ < 12 dB
	3 < Δ < 6 dB		Δ < 3 dB

Figure 10: Test Volume Ripple Data

The CW data in both vertical and horizontal polarization in figure 10 shows large deltas for the lower frequencies. As the frequency increased, the ripple values tend to decrease. This was due to the 6-foot RAM working more effectively at frequencies above 200 MHz where the RAM was at least one wavelength thick. The average ripple value across the CW data was 12 dB for vertical polarization and 11 dB for horizontal polarization. For the CW pulse data, the average ripple value was 5 dB for vertical polarization and 6 dB for horizontal polarization.

Comparing the CW to the CW pulse ripple data in figure 10 illustrates the improvements provided with hardware gating. In the vertically polarized CW data, several ripple values were above 20 dB and one as large as 47 dB were depicted. The vertically polarized CW pulse data had no values above 12 dB. This demonstrated the removal of multipath, resulting in a test zone with a ripple less than 7 dB. For horizontal polarization, the ripple data is similar in that the CW data has several values above 12 dB whereas all the CW pulse data is below 9 dB.

The EM field uniformity for the test volume was quantified in figure 11 by splitting field uniformity into four ranges and determining the percentage of data in each field uniformity range. In vertical polarization, the hardware gating equipment increases the amount of data within 6 dB of ripple range. Without hardware gating applied, 29 percent of the vertically polarized data is within 6 dB. When the signal is pulsed, 78 percent of the data are within this range. In horizontal polarization, there was only a small increase in the amount of data within the 6 dB range between the CW and CW pulse data. However, a significant improvement is that none of the CW pulse horizontal polarization data were above 12 dB while 42 percent of the CW data were above this limit. Hence, the hardware gating is effective since it decreased the amount of multipath in the test zone.

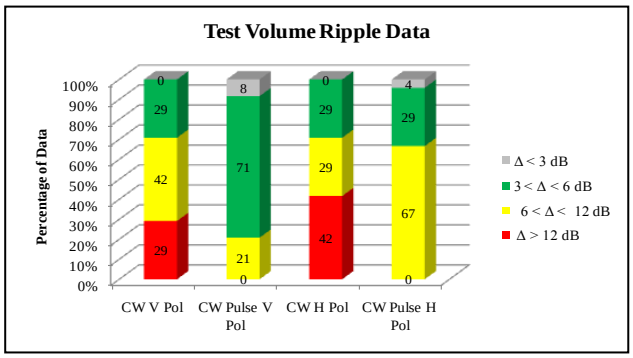

Figure 11: Test Volume Ripple Data Percentages

Overall Results

The multipath observed in the test volume for CW measurements between 100 and 500 MHz creates unpredictable field uniformity values ranging from 3 to 47 dB. This amount of variation creates measurement inaccuracies for antenna pattern and isolation measurements. The LFRI system created a more uniform field by reducing both the multipath present in the chamber and the amount of multipath measured at the SUT. The field uniformity in the test volume is between 2 and 9 dB for the CW pulse vertical and horizontal polarization data. Additional improvements in test zone ripple can be made by incorporating large 6 foot RAM fences in the Fresnel zone and increasing the path length of the ceiling reflection to move it out of the receive gate. Modification of this type is being analyzed and may be incorporated in a future date.

5.0 Summary

The LFRI test system, which incorporated three new low frequency test assets, 1) cross-log periodic antenna, 2) six-foot radar absorbing material, and 3) hardware gating, improved the EM field uniformity at frequencies between 100 and 500 MHz. This test effort characterized the EM test environment and demonstrated an increase in measurement accuracy in the test volume.

6.0 References

[1] AFFTC-TIH-10-03, Technical Information Handbook, 412 Electronic Warfare Group Benefield Anechoic Facility Low Frequency Range Improvement Test, 2010